La investigación reportada en esta tesis es parte de los programas de investigación del CICESE (Centro de Investigación Científica y de Educación Superior de Ensenada, B.C.).

La investigación fue financiada por el CONACYT (Consejo Nacional de Ciencia y Tecnología).

Centro de Investigación Científica y de Educación Superior de Ensenada, Baja California

Doctorado en Ciencias en Óptica Física

The optical properties of pyramidal prisms with applications in the generation of structured light

Tesis

para cubrir parcialmente los requisitos necesarios para obtener el grado de

Doctor en Ciencias

Presenta:

Carlos Ivan Ochoa Guerrero

Ensenada, Baja California, México

2022

Tesis defendida por

Carlos Ivan Ochoa Guerrero

y aprobada por el siguiente Comité

Dr. Kevin Arthur O'Donnell
Director de tesis

Dra. Veneranda Guadalupe Garcés Chávez

Dr. Eugenio Rafael Méndez Méndez

Dr. Roberto Machorro Mejía

Dr. Gabriel Cooper Spalding

Dr. Víctor Ruiz Cortés

Dra. Karina Garay Palmett
Coordinadora del Posgrado en Óptica

Dr. Pedro Negrete Regagnon
Director de Estudios de Posgrado

Resumen de la tesis que presenta Carlos Ivan Ochoa Guerrero como requisito parcial para la obtención del grado de Doctor en Ciencias en Óptica Física.

Las propiedades ópticas de prismas piramidales con aplicaciones en la generación de luz estructurada

Resumen aprobado por:

Dr. Kevin Arthur O'Donnell
Director de tesis

En esta tesis se presenta un estudio numérico de la luz estructurada producida por un haz de luz transmitido por un prisma piramidal simétrico. Utilizando la difracción de Fresnel se obtienen expresiones para las amplitudes de la luz difractada, las cuales son válidas para prismas piramidales truncados o con terminacion en pico con un número arbitrario de caras. Dichas expresiones son evaluadas facilmente de manera numérica y representan un avance significativo sobre los trabajos anteriores que utilizan un modelo discreto de ondas planas. La distribucion de la intensidad de la luz difractada es estudiada considerando un amplio rango de parámetros, y la eficiencia en la intensidad de las estructuras producidas es determinada debido a la unitaridad de las integrales de la difracción de Fresnel. Aunque en la mayoria de los resultados presentados se emplea un haz de luz láser Gausiano iluminando al prisma, tambien se demuestra como la teoria puede extenderse facilmente a modos de luz láser de orden superior. Se consideran posibles aplicaciones en atrapamiento óptico y se dan ejemplos en los que se puede obtener un número de puntos brillantes con similar intensidad que pudiese servir para atrapar simultaneamente varias partículas. También se consideran posibles aplicaciones en litografía en donde, bajo otras condiciones, se pueden producir patrones de luz periódica uniforme. Las ventajas prácticas en el empleo de prismas piramidales para las aplicaciones mencionadas anteriormente son excelente estabilidad y la eficiencia en la luz estructurada producida.

Palabras clave: Luz estructurada, Prismas Priamidales, Difracción de Fresnel

Abstract of the thesis presented by Carlos Ivan Ochoa Guerrero as a partial requirement to obtain the Doctor of Science degree in Optics.

The optical properties of pyramidal prisms with applications in the generation of structured light

Abstract approved by:

Dr. Kevin Arthur O'Donnell
Thesis Director

This thesis presents a numerical study of the structured light produced by a laser beam transmitted by a symmetric pyramidal prism. From the Fresnel formulation, expressions are obtained for the diffracted amplitudes that are valid for an arbitrary number of prism faces for both acute and flat-topped prisms. These expressions are readily evaluated numerically and are a significant advancement over the restrictive discrete plane wave models used in prior works. The distribution of intensity of the diffracted light is studied for a wide range of prism parameters, and the unitarity of Fresnel integrals allows the determination of the efficiency of the intensity structures produced, which is not possible with the plane wave model. While most of the results presented to consider a Gaussian laser beam illuminating the prism, it is demonstrated that the theory may be readily extended to higher-order laser modes. Applications in optical trapping are considered, and examples are given in which the intensity distributions contain a number of bright spots with similar intensity, as could be suitable for the simultaneous trapping of several particles. Also considered are applications in lithography and, under other conditions, cases are presented that produce uniform periodic intensity patterns. The practical advantages of employing pyramidal prisms in such applications are their excellent stability and their efficiency in producing structured light.

Keywords: Structured Light, Pyramidal Prisms, Fresnel Diffraction

Dedication

A Johanna y Febe por su paciencia, aliento y cariño

A mis padres por su apoyo incondicional

Acknowledgments

To Dr. Kevin O'Donnell for his guidance and sense of humor, and patience I don't know how many times he said to me the phrase *that is not what light does Carlos*, or all the endless discussions and conversations to aid me on my blackened days. For that and more thank you.

To Dra. Veneranda for her frank comments and her constant encouragement all along my stay in the Lab working with the group.

To committee members Professors Eugenio Mendez, Gabe Spalding, Roberto Machorro and Víctor Ruiz. Thank you for your valuable contributions, questions and comments in my PhD path.

To my beautiful wife Johanna for all that we have learned together.

A mis compañeros y amigos de CICESE, UNAM y UABC. Migue, Jano, Mitra, Tany, JC, Pixteen, Fer,Mey Jorge, Sammy, Aza,Angy, Yuni. Todos ustedes a su manera me inspiran, gracias por estar ahí y hacer las preguntas incomodas.

To the gang from instntly-klever, Ivan, Oscar Alen, Arnulfo and Lalo. Thanks to bear with me all the hard trips.

To my mystical friends Cohen and María. Love you guys.

To the Antesala community, thank you all for your warm welcome and kind treatment.

Al Centro de Investigación Científica y de Educación Superior de Ensenada, Baja California por permitirme realizar mis estudios de doctorado y a los profesores del posgrado por su guía y enseñanzas.

Al Consejo Nacional de Ciencia y Tecnología (CONACyT) por brindarme el apoyo económico para realizar mis estudios de doctorado.

To you reader.

Table of contents

List of figures

Figure Page

Chapter 1. Introduction

This thesis develops the theoretical foundations necessary to understand the structured light produced when a laser beam is transmitted by a symmetric pyramidal prism. The study is based on the derivation and numerical evaluation of expressions for the diffracted amplitude within the Fresnel approximation. In the Fresnel field after the prism, it is shown that structured light is produced that, depending on parameters, can take on a wide variety of forms. By varying and eventually optimizing the parameters, cases are found in which the structured light produced can be useful in a number of important applications.

The simplest pyramidal prism considered here has only two faces, which is a case well-known historically as a Fresnel biprism and is one of the earliest methods of producing two-beam interference (Jenkins and White, 1976). The biprism may readily be generalized to a prism having 3 or more faces, which meet at a point at the prism center. Just as for the biprism, the light transmitted by such a pyramidal prism will exhibit interference, although it should be expected that a prism having many sides will produce an interference pattern considerably more complex than that of a biprism.

Pyramidal prisms have been studied previously, along with flat-topped versions in which the apex of the pyramid has been cut away and replaced by a flat prism face. For both prism types, Lei *et al.* (2006) have used a model of the transmitted field as a superposition of a finite set of plane waves, with each prism face associated with a plane wave traveling in the direction of its corresponding refracted ray. Flat-topped prisms have been widely employed in lithography to produce nanostructures in 2D and 3D (Wang *et al.*, 2003; Wu *et al.*, 2005; Pang *et al.*, 2006; Juodkazis *et al.*, 2009; Jiang *et al.*, 2013; Park and Yang, 2013; Jeon *et al.*, 2018). Applications include photonic crystals, metamaterials, and nanoelectronics (Ji-Hyun *et al.*, 2007; Burrow and Gaylord, 2011). Throughout this work, plane wave models like that of Ref. (Lei *et al.*, 2006) have been used to provide insight into the structures produced.

Here, a novel approach is employed to obtain a more complete understanding of the interference produced by pyramidal prisms. The point of view taken is that the distributions may be considered to be structured light (Rubinsztein-Dunlop *et al.*, 2017; Forbes *et al.*, 2021), since the output fields are three-dimensionally sculpted in amplitude and phase. To obtain interferometric stability, pyramidal prisms are often used by illuminating them with a spatial laser mode, whose wavefront is intercepted by the prism faces (Wang *et al.*, 2003; Wu *et al.*, 2005; Jiang *et al.*, 2013; Park and Yang, 2013; Jeon *et al.*, 2018; Stay *et al.*, 2011; Brundrett *et al.*, 1998; Savas *et al.*, 1995; Kondo *et al.*, 2001); the transmitted wavefront segments are refracted into different directions and then propagate to an overlap region after the prism. Thus the situation is clearly a diffraction problem so all previous work using a discrete plane wave model necessarily has limitations. Fresnel diffraction integrals are employed here and, by using the symmetries that the prism presents, closed-form solutions are obtained for the diffracted field for an arbitrary finite number of prism faces. The expressions obtained require numerical integration in but one variable, and so are straightforward to evaluate.

The field of structured light has rapidly expanded in recent years, and a number of methods of producing structured light have been recently developed (Forbes *et al.*, 2021; Rubinsztein-Dunlop *et al.*, 2017). Still, the proposal made in this thesis to use pyramidal prisms to produce structured light is, strictly speaking, novel; thus wide exploration is necessary to find cases useful in applications. A common application of structured light is in optical trapping (Otte and Denz, 2020; Yang *et al.*, 2021), and some of the calculations presented in this thesis are directed toward this application. In particular, it is demonstrated here that the optical power transmitted by a prism can be efficiently distributed into a number of nearly identical spots, which could thus form an array of traps; the efficiency is important since the spatial modulators commonly used in trapping often produce significant losses. Other calculations presented here are more geared toward lithography, as was discussed earlier. In particular, calculations are presented in which fairly uniform periodic patterns are efficiently produced, as can be essential in lithography. Throughout all these examples, the diffraction approach allows one to calculate the field structure produced by given configuration, and to then vary experimentally accessible parameters until an optimal result is obtained. This has not been possible in previous works.

An important aspect of a pyramidal prism is its monolithic nature. Once fabricated, it is extremely robust and its angles and internal optical paths will not vary, with the consequence that the interference patterns it produces will be extremely stable. This should be contrasted with approaches using beamsplitters, for which angular alignment and interferometer path lengths are difficult to maintain (Ji-Hyun *et al.*, 2007; Burrow and Gaylord, 2011). Thus a pyramidal prism could be essential for industrial or production applications, or in any other case where extreme stability and reproducibility is required.

1.1 Hypothesis

That the structured light produced by a pyramidal prism can be studied by appropriate application of diffraction theory, using the symmetries present. Further, the light distributions can show potential utility in lithography, optical trapping, and other applications.

1.2 Justification

Before the current work, the models for structured light generation by prisms consisted of interfering plane waves. Such models provide little information about the optical power in a region of interest, the variations in intensity along the optical axis, or the uniformity of the features produced.

That is why the current work proposes to investigate the generation of structured light using Fresnel diffraction theory to gain more information than the plane wave models of the literature. By comparing the new results with previous models, this work proposes two applications for which the plane wave model presents limitations.

1.3 Objectives

- Use Fresnel diffraction theory applied to a Gaussian beam transmitted by a multi-faced pyramidal prism.
- Develop the theory for flat-topped pyramidal prisms.
- Develop results that can be useful in lithography or optical trapping.

1.4 Thesis outline

The structure of this thesis is as follows. Chapter 2 begins with a discussion of Fresnel diffraction theory. It then presents a theoretical study for the Fresnel biprism and multi-faced pyramidal prisms. Chapter 3 presents numerical calculations of the diffracted intensity for acute prisms, and presents comparisons with previous works in the literature. Chapter 4 presents numerical calculations for flat-topped pyramidal prisms and some comparisons between acute and flat-topped pyramidal prisms. In Chapter 5 is presented an expanded discussion on the nature of variations in intensity along the optical propagation axis for acute and flat-topped prisms. Chapter 6 presents our approach to optimize a distribution of small spots, where the goal considered here is to produce multiple spots with nearly the same power. This optimization alone produces results attractive to both optical trapping and lithography. Chapter 7 deals with the possibility of producing uniform interference patterns which has potential applications in lithography. Finally, Chapter 8 highlights the results from our investigation, clearly comparing our hypothesis and objectives, emphasizing the implications of our results, and proposing the direction of future research.

Chapter 2. Fresnel diffraction theory for pyramidal prisms

Consider a diffracting aperture in the ξ-η plane illuminated by a Gaussian beam propagating in the positive z direction. We calculate the diffracted field in the x-y plane, which is parallel to the ξ-η plane and a distance z from it as shown in Fig. 1.

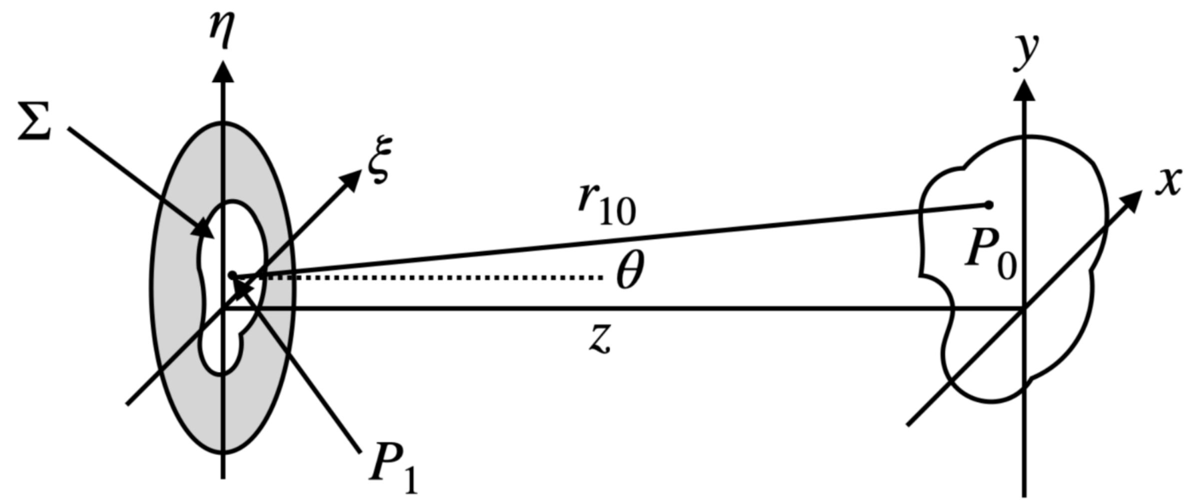

Figure 1. Diffraction geometry used.

The complex amplitude at a point P_0 in the x-y plane given by the diffraction integral Goodman (2017)

$$U(P_0) = \frac{1}{i\lambda} \iint_{\Sigma} U(P_1) \frac{e^{ikr_{10}}}{r_{10}} \cos\theta d\xi d\eta, \tag{1}$$

where Σ is the integration area, P_1 and P_0 are points that lay in the ξ-η plane and x-y plane, respectively, $k = \frac{2\pi}{\lambda}$, λ is the wavelength, and θ is the angle between the outward normal to the x-y plane and the line that connects P_1 to P_0. In Eq.(1) $\cos\theta = \frac{z}{r_{10}}$, and z is the propagation distance. We then write the complex amplitude at a point in the x-y plane as

$$U(x, y) = \frac{z}{i\lambda} \iint_{\Sigma} U(\xi, \eta) \frac{e^{ikr_{10}}}{r_{10}^2} d\xi d\eta, \tag{2}$$

where $r_{10} = \sqrt{z^2 + (x-\xi)^2 + (y-\eta)^2} = z\sqrt{1 + \left(\frac{x-\xi}{z}\right)^2 + \left(\frac{y-\eta}{z}\right)^2}$. The binomial expansion for a square root is

$$\sqrt{1+b} = 1 + \frac{1}{2}b - \frac{1}{8}b^2 + \cdots \tag{3}$$

where $b << 1$. Then the kr_{10} term can be expanded as

$$kr_{10} = kz\left[1+\frac{1}{2}\left(\frac{x-\xi}{z}\right)^2+\frac{1}{2}\left(\frac{y-\eta}{z}\right)^2-\frac{1}{8}\left\{\left(\frac{x-\xi}{z}\right)^2+\left(\frac{y-\eta}{z}\right)^2\right\}^2\right]. \quad (4)$$

Now we assume that the maximum phase change induced by the third term of Eq.(4) is much less than unity so that

$$\frac{kz}{8}\left[\left(\frac{x-\xi}{z}\right)^2+\left(\frac{y-\eta}{z}\right)^2\right]^2 << 1. \quad (5)$$

Therefore it is found that

$$\frac{k}{8}\left[(x-\xi)^2+(y-\eta)^2\right]^2 << z^3, \quad (6)$$

which is the condition that z must satisfy. Neglecting the last term inside the curly braces from Eq.(4) is possible to rewrite the complex amplitude in the x-y plane at a distance z as

$$U(x,y) = \frac{e^{ikz}}{i\lambda z}\iint_{-\infty}^{\infty} U(\xi,\eta)e^{\frac{ik}{2z}\left[(x-\xi)^2+(y-\eta)^2\right]}d\xi d\eta. \quad (7)$$

By writing the amplitude that describes a Gaussian beam in the form $U_G(\xi,\eta) = e^{-\left(\frac{\xi^2+\eta^2}{w^2}\right)}e^{\frac{ik(\xi^2+\eta^2)}{2R}}$, where R is the radius of curvature of the Gaussian beam, w the beam width at the diffracted aperture plane ξ-η.

By expressing the amplitude in the case of the pyramidal prisms studied here, as $U(\xi,\eta) = U_G(\xi,\eta) \times t_p(\xi,\eta)$, so the complex amplitude is

$$U(x,y) = \frac{e^{ikz}}{i\lambda z}\iint_{-\infty}^{\infty} t_p(\xi,\eta)e^{-\left(\frac{\xi^2+\eta^2}{w^2}\right)}e^{\frac{ik(\xi^2+\eta^2)}{2R}}e^{\frac{ik}{2z}\left[(x-\xi)^2+(y-\eta)^2\right]}d\xi d\eta, \quad (8)$$

where $t_p(\xi,\eta)$ is the amplitude transmittance of the relevant prism, which may be an acute or a flat-topped pyramidal prism. The following sections present the results of the diffraction of a Gaussian beam transmitted by such prisms.

Throughout all development in this thesis, polarization effects are not taken into account, which is common in treatments employing Fresnel diffraction. In particular, all cases studied consider prisms producing small refraction angles, hence polarization effects are negligible. However, in the extreme case of a prism producing steep refraction angles, the theory developed here may be adapted as will be discussed later.

2.1 Fresnel biprism

A Fresnel biprism (also known as a Fresnel double prism) modifies the beam that illuminates the biprism in the following manner. According to Fig. 2 the upper portion of the beam is refracted downward, and the lower portion upwards. In the superposition region, geometrical interference occurs, shown as the diamond-shaped domain.

The amplitude transmittance for the upper part of the prism is Saleh and Teich (1991)

$$t_p(\xi, \eta) = e^{-ik\eta \sin\theta}, \tag{9}$$

and the amplitude transmittance for the lower part is

$$t_p(\xi, \eta) = e^{ik\eta \sin\theta}. \tag{10}$$

Instead of using Eqs. (9-10), both can be combined using an absolute value that accounts for both faces and obtains the amplitude transmittance for a Fresnel biprism as

$$t_{Fb}(\xi, \eta) = e^{-i\frac{2\pi}{\lambda}|\eta| \sin\theta} \tag{11}$$

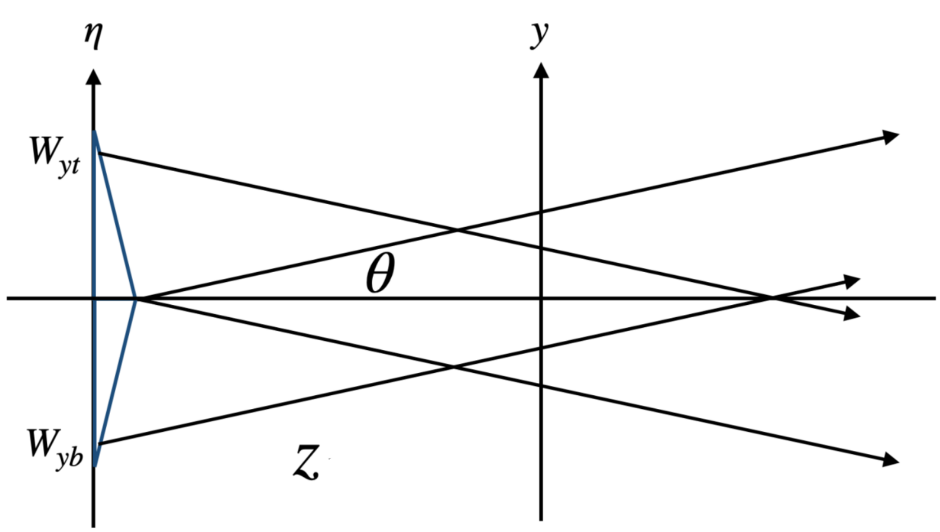

Figure 2. The location of the prism is in the ξ-η plane, x-y plane at z is the diffracted field. The diamond in the diagram represents the superposition region where interference occurs. The x and ξ axes point inwards. θ is the refraction angle, and W_{yt} and W_{yb} correspond to the aperture distance from center to top and center to the bottom of the prism, respectively.

Now substituting Eq.(11) into Eq.(8), we get the Fresnel diffraction integral for a Fresnel biprism as

$$U(x,y)=\frac{e^{ikz}}{i\lambda z}\int_{-W_{yb}}^{W_{yt}}\int_{-W_{xl}}^{W_{xr}} e^{-\frac{\xi^2+\eta^2}{w^2}+\frac{ik(\xi^2+\eta^2)}{2R}-ik|\eta|\sin\theta+\frac{ik}{2z}[(x-\xi)^2+(y-\eta)^2]}d\xi d\eta \tag{12}$$

Note that we are taking the integration limits with a rectangular aperture in the ξ-η plane, with W_{xl}, W_{xr}, W_{yt},W_{yb} being the distances from the center to each side of the aperture. In order to consider the whole space, take $W_{xl}\to\infty$, $W_{xr}\to\infty$, $W_{yt}\to\infty$,$W_{yb}\to\infty$. Then this integral may be split as the product of two integrals on ξ and η, and get a closed-form solution in terms of error functions in the x-y plane as:

$$U(x,y)=U(x)\left[U_t(y)+U_b(y)\right], \tag{13}$$

where the x-component of the amplitude is

$$U(x)=\kappa_x\left[\mathrm{erf}(\xi_l)+\mathrm{erf}(\xi_r)\right], \tag{14}$$

where $\mathrm{erf}()$ is the Error function, and

$$\kappa_x=\frac{\sqrt{i\pi Rz}we^{-\frac{k(2R+ikw^2)x^2}{2kw^2(R-z)+4iRz}}}{\sqrt{2kw^2(R-z)+4iRz}},$$

$$\xi_l=\frac{(-1)^{3/4}\left(2iRW_{xl}z+kw^2(RW_{xl}-Rx-W_{xl}z)\right)}{w\sqrt{2Rz(kw^2(R-z)+2iRz)}},$$

$$\xi_r=\frac{(-1)^{3/4}\left(2iRW_{xr}z+kw^2(RW_{xr}-Rx-W_{xr}z)\right)}{w\sqrt{2Rz(kw^2(R-z)+2iRz)}},$$

the amplitude contribution from the upper part is

$$U_t(y)=\kappa_{yt}\left[\mathrm{erf}(\eta_{t1})+\mathrm{erf}(\eta_{t2})\right], \tag{15}$$

where

$$\kappa_{yt}=-\frac{(-1)^{3/4}\sqrt{\pi Rz}we^{\frac{i\left(ky^2-\frac{Rw^2(ky\lambda+2\pi z\sin\theta)^2}{(2iRz+kw^2(R+z))\lambda^2}\right)}{2z}}}{\sqrt{4iRz+2kw^2(R+z)}},$$

$$\eta_{t1} = \frac{\left(\frac{1}{2}+\frac{i}{2}\right)\sqrt{R}w(ky\lambda + 2\pi z\sin\theta)}{i\lambda\sqrt{z(2iRz + kw^2(R+z))}},$$

$$\eta_{t2} = \frac{(-1)^{1/4}(2iRW_{yt}z\lambda + kw^2(R(W_{yt}-y) + W_{yt}z)\lambda - 2\pi Rw^2 z\sin\theta)}{iw\lambda\sqrt{4iRz + 2kw^2(R+z)}},$$

and the amplitude contribution from the lower part is

$$U_b(y) = \kappa_{yb}\left[\mathrm{erf}(\eta_{b1}) + \mathrm{erf}(\eta_{b2})\right], \tag{16}$$

where

$$\kappa_{yb} = -\frac{(-1)^{3/4}\sqrt{\pi Rz}we^{\frac{i\left(ky^2 - \frac{Rw^2(ky\lambda - 2\pi z\sin\theta)^2}{(2iRz+kw^2(R+z))\lambda^2}\right)}{2z}}}{\sqrt{4iRz + 2kw^2(R+z)}},$$

$$\eta_{b1} = \frac{\left(\frac{1}{2}+\frac{i}{2}\right)\sqrt{R}w(-ky\lambda + 2\pi z\sin\theta)}{i\lambda\sqrt{z(2iRz + kw^2(R+z))}},$$

$$\eta_{b2} = \frac{(-1)^{1/4}(2iRW_{yb}z\lambda + kw^2(R(W_{yb}+y) + W_{yb}z)\lambda - 2\pi Rw^2 z\sin\theta)}{iw\lambda\sqrt{4iRz + 2kw^2(R+z)}}.$$

Note that Eq.(13) is an analytic solution that involves six error functions. It contains much physical information, such as Gaussian beam parameters, limiting apertures, and the effect of the biprism, thus now it is possible to compute the intensity in any desired plane.

2.2 Pyramidal prism

The approach taken to addressing a complete pyramidal prism is to use its symmetry and concentrate on a single facet of the prism. We compute the diffracted amplitude distribution produced by an infinite wedge on the ξ-η plane, this wedge represent one single facet of the prism, as shown in Fig. 3(c). This wedge represents one face of a flat-top pyramid, and it also accounts for the case of an acute pyramid when $\xi_\circ = 0$.

From the Fresnel diffraction integral of Eq.(8) it is possible to calculate the amplitude distribution $U_1(x, y)$ in the observation plane shown in Fig. 4. The distribution comes from the wedge with an internal angle of $\Delta\phi$, located at the ρ-φ plane. We then write the Fresnel diffraction integral at the r-ϕ

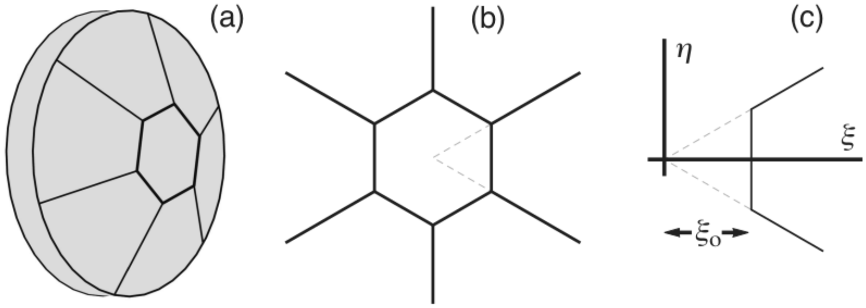

Figure 3. (a) Flat-topped pyramidal prism having six radial sides. (b) Axial view of the prism showing the hexagonal cap. (c) Face on the right of (b) with (ξ, η) axes introduced; the wedged region for $\xi \geq \xi_0$ is covered by expression (17), note that the expression is now in cylindrical coordinates and $\xi_\circ$ is now $\rho_\circ$. Dashed lines in (b) and (c) indicate limits of the cap region covered by term pairs of a given index m in Eq. (25).

plane in cylindrical coordinates for this wedge as

$$\begin{aligned} U_1(r,\phi) = \;& \frac{e^{ikz}}{i\lambda z}\int_{-\Delta\phi}^{\Delta\phi} \\ \times\;& \left[\int_0^{\frac{\rho_0}{\cos\varphi}} e^{-\left(\frac{\rho^2}{w^2}\right)} e^{\frac{ik(\rho^2)}{2R}} e^{\frac{ik}{2z}\left[r^2\sin^2(\phi-\varphi)+[\rho-r\cos(\phi-\varphi)]^2\right]}\rho d\rho \right. \\ +\;& \left. \int_{\frac{\rho_0}{\cos\varphi}}^{\infty} t_1(\rho,\varphi) e^{-\left(\frac{\rho^2}{w^2}\right)} e^{\frac{ik(\rho^2)}{2R}} e^{\frac{ik}{2z}\left[r^2\sin^2(\phi-\varphi)+[\rho-r\cos(\phi-\varphi)]^2\right]}\rho d\rho\right] \\ \times\;& d\varphi. \end{aligned} \tag{17}$$

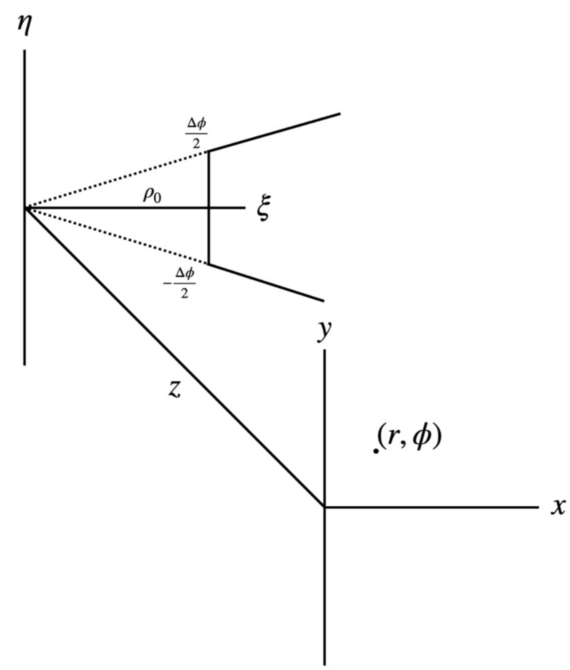

Figure 4. A wedged region that represents one face of an N-faced flat-top pyramid.

Where the $\rho = \sqrt{\xi^2+\eta^2}$ and $\varphi = \arctan\frac{\eta}{\xi}$, are the aperture coordinates and $r = \sqrt{x^2+y^2}$ and

$\phi = \arctan\frac{y}{x}$ the diffracted plane cylindrical coordinates. The flat-top part extends from the origin up to a distance ρ_0 and $t_1(\rho,\varphi)$ is the transmittance of the wedge, which is given by

$$t_1(\rho,\varphi) = e^{-ik(\rho-\frac{\rho_0}{\cos\varphi})\cos\varphi\sin\theta}, \tag{18}$$

where θ is the angle of refraction.

Solving the ρ integral that runs from the origin to $\frac{\rho_0}{\cos\varphi}$

$$I_1(\varphi,r,\phi) = kw^2 e^{-k\frac{(kw^2\beta^2-i\alpha r^2)}{2z\alpha}}\left(\frac{T_1+T_2}{4\pi z\alpha^2}\right), \tag{19}$$

and then the second integral that goes from $\frac{\rho_0}{\cos\varphi}$ to infinity, to get

$$I_2(\varphi,r,\phi) = -\frac{2iz\alpha kw^2}{4\pi\alpha^2 z}\left(e^{-k\frac{(kw^2\beta^2-i\alpha r^2)}{2z\alpha}+\frac{(-ia\alpha+kw^2\beta)^2}{2w^2z\alpha}+kw\beta\sqrt{2\pi z\alpha}}\right)\text{erfc}\left[\frac{a\alpha+ikw^2\beta}{w\sqrt{2z\alpha}}\right] \tag{20}$$

where

$$T_1 = -2iz\alpha\left(e^{\frac{(kw\beta)^2}{2z\alpha}} - e^{\frac{(-i\frac{\rho_0}{\cos\varphi}\alpha+kw^2\beta)^2}{2w^2z\alpha}}\right),$$

$$T_2 = k\sqrt{2\pi z\alpha}w\beta\left(\text{erf}\left[\frac{\frac{\rho_0}{\cos\varphi}\alpha+ikw^2\beta}{w\sqrt{2z\alpha}}\right] - \text{erf}\left[\frac{ikw\beta}{\sqrt{2z\alpha}}\right]\right),$$

$\beta = r\cos(\varphi-\phi)+z\cos(\varphi)\sin\theta$, $\alpha = 2z-ikw^2(1+\frac{z}{R})$, and $\text{erfc}(x) = 1-\text{erf}(x)$ is the complementary Error function.

The diffraction amplitude for the first wedge is then

$$U_1(r,\phi) = \frac{e^{ikz}}{i\lambda z}\int_{-\frac{\Delta\phi}{2}}^{\frac{\Delta\phi}{2}}[I_1(\varphi,r,\phi)+I_2(\varphi,r,\phi)]d\varphi. \tag{21}$$

Now it is possible to calculate the amplitude on any point of the r-ϕ plane, the amplitude on the point (r_0,ϕ_0) in Fig. 4 is $U_1(r_0,\phi_0)$.

Consider now a second wedge having the exact dimensions as the first one but rotated by $\Delta\phi$ degrees clockwise about the z-axis as shown in Fig. 5.

To calculate the amplitude produced by the second wedge $U_2(r_0,\phi_0)$ at the point (r_0,ϕ_0), solve the integral

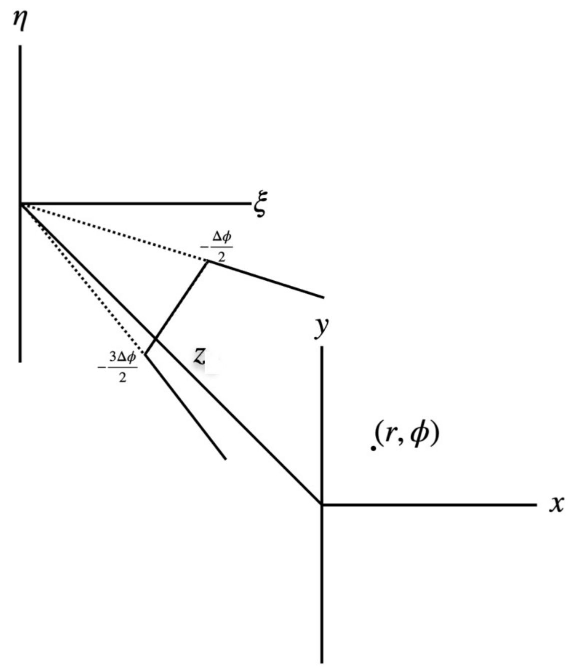

Figure 5. Position of a second wedge that represents the second face of an n-faced flat-top pyramid adjacent to the first wedge shown in Fig. 4.

$$U_2(r_0,\phi_0) = \frac{e^{ikz}}{i\lambda z}\int_{-\frac{3\Delta\phi}{2}}^{-\frac{\Delta\phi}{2}} [I_1(\varphi, r_0, \phi_0) + I_2(\varphi, r_0, \phi_0)]d\varphi. \tag{22}$$

However, suppose that one now rotates both the wedge and the point in the diffraction plane counter-clockwise by $\Delta\phi$ as in Fig. 6. Then it is immediately apparent that the physical situation is identical to that of Fig. 4, but with the *field* point rotated by $\Delta\phi$. It thus follows that $U_2(r_0,\phi_0)$ in Fig. 5 is given by

$$U_2(r_0,\phi_0) = U_1(r_0,\phi_0+\Delta\phi) \tag{23}$$

It follows that the amplitude of a third wedge would be $U_3(r_0,\phi_0) = U_1(r_0,\phi_0+2\Delta\phi)$. In general, for the mth wedge

$$U_m(r_0,\phi_0) = U_1(r_0,\phi_0+(m-1)\Delta\phi)\,. \tag{24}$$

The total amplitude $A(r_0,\phi_0)$ produced by the entire prism is the sum of the amplitudes produced by

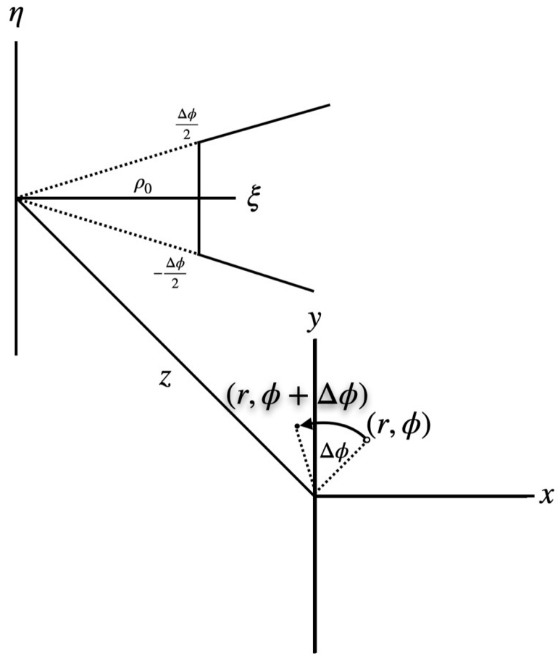

Figure 6. Position of a second wedge from Fig. 5 rotated $\Delta\phi$ degrees counterclockwise, and the evaluated point rotated by the same amount.

its N faces as

$$A(r_0, \phi_0) = \sum_{m=1}^{N} U_m(r_0, \phi_0) = \sum_{m=1}^{N} U_1(r_0, \phi_0 + (m-1)\Delta\phi)\,, \tag{25}$$

with $\Delta\phi = 2\pi/N$.

Thus Eq. 25 represents a complete solution for the Fresnel diffraction pattern produced by a prism having N identical radial faces and a flat top. It is possible to obtain an acute pyramid when the minimum half-width of the pyramid cap takes the value $\rho_0 = 0$.

By writing Eq. 25 in terms of the flat cap and the sloping side, to get an expression that allows generalizing the results obtained so far. It is possible to rewrite the integrand terms $\frac{e^{ikz}}{i\lambda z}\left(I_1(\varphi, r_0, \phi_0) + I_2(\varphi, r_0, \phi_0)\right)$ from Eq.2.2 as single expression and making explicit the θ dependency as

$$\begin{aligned} H(r, \phi, \varphi, \rho_0, \theta) \;\; = \;\; & \left[\frac{A_\circ k w^2 z}{\pi \alpha_1^{3/2}}\right] e^{ik[\rho_0 \sin\theta + r^2/(2z)]} e^{-k^2 w^2 \beta_1^2/\alpha_1} \\ & \times \left\{ \sqrt{\pi} k w \beta_1 \left[\mathrm{erf}\left(\frac{\gamma_1}{\sqrt{\alpha_1}}\right) - 1 \right] - i\sqrt{\alpha_1} e^{-\gamma_1^2/\alpha_1} \right\}, \end{aligned} \tag{26}$$

where $\alpha_1 = 2z[2z - ikw^2(1 + z/R)]$, $\beta_1 = r\cos(\varphi - \phi) + z\cos\varphi\sin\theta$, and $\gamma = ikw\beta_1 + \rho_0\alpha_1/(2wz\cos\varphi)$.

For convenience, the external factor $(i\lambda z)^{-1}$ of expression 17, has been incorporated into Eq. 26, so that expression 17 is now

$$\int_{-\Delta\phi/2}^{\Delta\phi/2} H(r,\phi,\varphi,\rho_0,\theta)d\varphi. \tag{27}$$

This integral may not be done in closed form but is ready for evaluation through numerical integration, following the development used earlier to obtain equation 25. For the other radial prism faces in Fig. 3(b), consider the face just below that discussed previously. From symmetry, it becomes apparent that this second face produces an amplitude at the field point (r,ϕ) identical to the amplitude that the first face produces at the field point $(r,\phi+\Delta\phi)$. More generally, the N-fold symmetry of the problem guarantees that the nth face produces an amplitude at (r,ϕ) identical to that of the first face at $(r,\phi+(n-1)\Delta\phi)$. Thus, for N such faces, the total diffracted field at a distance z from the prism is the sum of these contributions as

$$\mathcal{A}_{\mathsf{dc}}(r,\phi,z) = \sum_{n=1}^{N}\int_{-\Delta\phi/2}^{\Delta\phi/2} H[r,\phi+(n-1)\Delta\phi,\varphi,\rho_0,\theta]d\varphi, \tag{28}$$

which is our solution for a prism having a dark central cap. If the prism instead has N radial faces that meet at an acute point at the center of the prism, it is seen from Fig. 3 (c) that $\rho_0 = 0$, resulting in the total diffracted amplitude

$$\mathcal{A}_{a}(r,\phi,z) = \sum_{n=1}^{N}\int_{-\Delta\phi/2}^{\Delta\phi/2} H[r,\phi+(n-1)\Delta\phi,\varphi,0,\theta]d\varphi. \tag{29}$$

If the prism has a flat, transmitting cap, the resulting amplitude $\mathcal{A}_{\mathsf{tc}}(r,\phi,z)$ may be found by adding $\mathcal{A}_{\mathsf{dc}}(r,\phi,z)$ to the diffracted amplitude produced by the cap, which has the shape of a regular convex polygon with N sides. Is it possible to write $\mathcal{A}_{\mathsf{tc}}(r,\phi,z)$ in the form

$$\begin{aligned}\mathcal{A}_{\mathsf{tc}}(r,\phi,z) &= \mathcal{A}_{\mathsf{dc}}(r,\phi,z) \\ &+ \sum_{n=1}^{N}\int_{-\Delta\phi/2}^{\Delta\phi/2}\{H[r,\phi+(n-1)\Delta\phi,\varphi,0,0] \\ &- H[r,\phi+(n-1)\Delta\phi,\varphi,\rho_0,0]d\varphi\}.\end{aligned} \tag{30}$$

For a given n in Eq. 30, the two terms within the integral produce the diffracted amplitude due to a wedged region from zero to infinity, minus that from $\rho_0/\cos\varphi$ to infinity, with both having no deflection angle since $\theta = 0$. Fig. 3 shows the resulting triangular effective domain; to obtain the diffracted amplitude of the polygonal prism cap sum over n in Eq. 30. Thus the results here of Eqs. 26-30 cover several realistic situations. Further, the general approach developed here may be applied even more widely. For instance, the laser mode incident on the prism need not be Gaussian as assumed earlier; one such example will be given here in Chapter 7 for a Hermite Gaussian incident mode.

2.3 Plane wave model for pyramidal prisms

In the following computations, we compare with a simplified model in which each prism face is associated with a plane wave propagating in a different direction Lei *et al.* (2006). For a flat-topped pyramid, this approach models the total diffracted amplitude as the plane wave sum

$$A_{PW}(x,y,z) = A_0 e^{ikz} + \sum_{n=1}^{N} A_0 e^{i\left(\overrightarrow{k}_n \cdot \overrightarrow{r} + \delta\right)}, \tag{31}$$

where $\overrightarrow{r} = (x,y,z)$, and A_0 is here the plane-wave amplitude. The first term of Eq.31 is a wave traveling along the z axis, which the model associates with the prism cap. The wave vectors $\overrightarrow{k}_n$ in the sum of Eq.31 lie on a cone and have directions identical to the rays refracted toward the z axis by the N radial prism faces. For an acute prism, we remove the first term of Eq.31, and the model is then

$$A_{PW}(x,y.z) = \sum_{n=1}^{N} A_0 e^{i\overrightarrow{k}_n \cdot \overrightarrow{r}}, \tag{32}$$

where the phase δ has been dropped.

Generally, the plane wave model may be suitable in cases with a wide incident beam and broad prism faces in a region having good overlap between the light from the faces. Still, this model completely neglects relevant effects of diffraction, which is particularly significant from prism edges, and it provides little insight into the detailed structure of the overlap region. Further, since the plane wave model carries infinite power, it is impossible to consider efficiency issues. On the other hand, the incident laser modes employed in this work contain power $\pi w^2 |A_0|^2/2$. Since Fresnel integrals are unitary, it is straightforward to integrate the diffracted intensity and thus determine the relative power within any region of interest.

2.4 Overlap diagrams

For the numerical results presented in the following chapters, the intensity curves in the x-y plane have an accompanying inset that illustrates the amount of overlap predicted by geometrical optics. For example, Fig. 7 displays a three-faced acute pyramidal prism overlap diagram for three different positions. Here are drawn wedges having the shape of each radial prism face, with an outer edge drawn as an arc at the $1/e^2$ point w of beam amplitude. Each wedge is displaced a radial distance $z\tan\theta$ toward the optical axis, as is consistent with geometrical propagation. In addition, when applicable, a dashed circle is added that indicates the region contained in the associated circular plot of intensity.

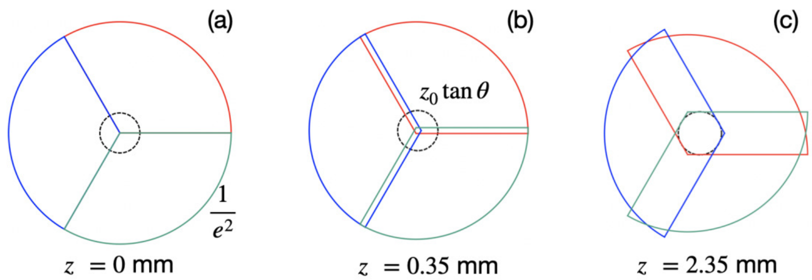

Figure 7. Overlap diagrams for an acute pyramidal prism of $N = 3$ sides. With an outer edge drawn as an arc at the $1/e^2$. Each wedge is displaced a radial distance $z\tan\theta$ toward the optical axis. Each case is evaluated at different distances (a) $z = 0$ mm, (b) $z = 0.35$ mm, (c) $z = 2.35$ mm to illustrate the radial displacement towards the optical axis of each wedge.

Chapter 3. Numerical results for acute pyramidal prisms

This chapter presents numerical results based on the theory from Chapter 2 to demonstrate typical intensity distributions for acute pyramidal prisms. The parameters considered for the following set of results are a refractive angle of $\theta = 0.5°$, a wavelength of $\lambda = 633$ nm, and a Gaussian width $w = 250$ μm. All the results possess a symmetry equivalent to the number of faces of each pyramid. Throughout all the cases, the intensity presents the N-fold symmetry as expected, and the typical interference features are $\approx 70\,\mu$m wide, of the order of $\lambda/\sin\theta$.

3.1 Two-faced prism

For the case of a biprism as shown in Fig. 8, an overlap region behind the prism along the optical axis is defined. Figure 8 represents the geometrical overlap where two halves of a Gaussian beam interfere, where γ is the internal angle of the prism, and θ is the refraction angle. Inside the overlap region, the interference pattern obtained from this configuration resembles the fringes from a double-slit experiment. The following sections analyze the intensity in the x-y plane at distances $z = 5.5$ mm, and then at $z = 14.3$ mm.

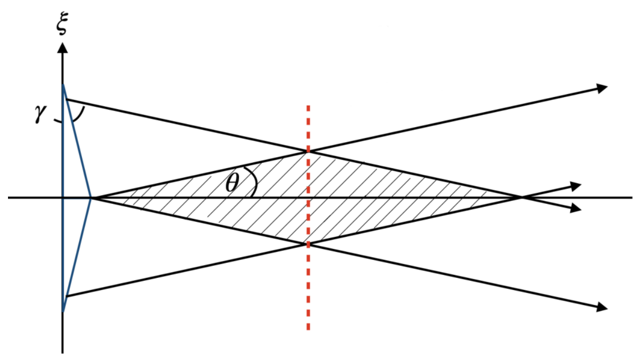

Figure 8. Light propagation behind a biprism with internal angle γ and deflection angle $\theta = \gamma(n_i - 1)$, where here n_i corresponds to the refractive index of the prism material, with the cross-hatched area denoting the region of geometrical overlap. The dashed red line corresponds to the position having maximum overlap.

Figure 9 shows the intensity along the optical axis. Note that, after an initial rise, the intensity falls with apparent oscillations, now referred to as intensity variation. The maximum of these oscillations located at $z = 5.5$ mm. Employing Eq. (25) to calculate the intensity $I_a \equiv |A_a|^2$ at a distance $z = 5.5$ mm in the x-y plane shown in Fig. 10 which exhibits a bright fringe in the middle with an intensity $\approx 5|A_0|^2$. Also, it is an even function in x.

Figure 10(a) shows the intensity profile on the x-axis at a distance $z = 5.5$ mm. Three central fringes are on the overlap region. The lack of contrast from the rest of the fringes as x increases in the figure

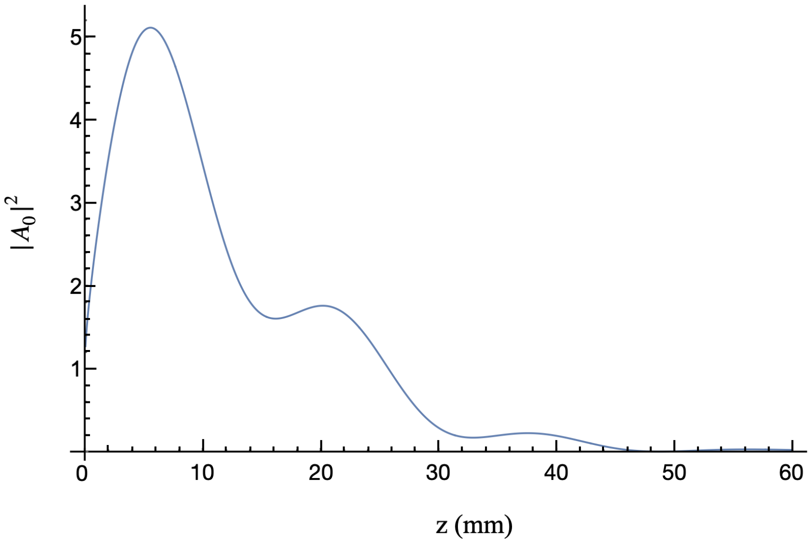

Figure 9. Intensity along the z-axis for a biprism with $\lambda = 633$ nm, $\theta = 0.5°$, and $w = 0.25$ mm. The location of the maximum is at $z = 5.5$ mm.

because they fall outside the geometrical overlap region. The maximum intensity is up to five times the intensity of the input beam. Note there are also two places located approximately at ± 20 μm where there is almost no light.

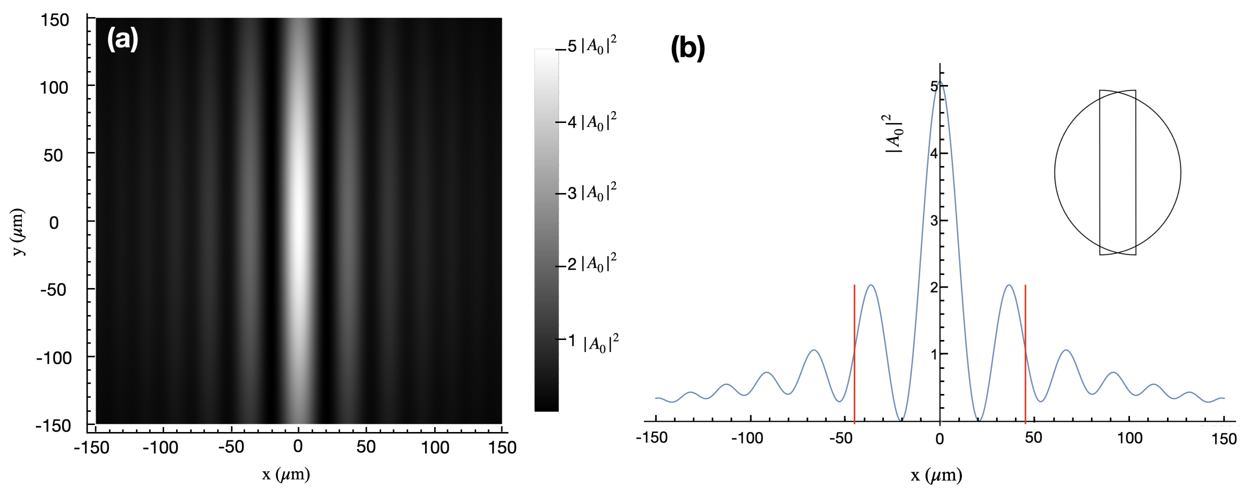

Figure 10. (a) Intensity in the x-y plane for a biprism with $z = 5.5$ mm, $\lambda = 633$ nm, $\theta = 0.5°$, and $w = 0.25$ mm. The sidebar indicates the intensity of the fringes, where the maximum is $\approx 5|A_0|^2$ from the input beam. **(b)** Intensity profile along the x-axis of (a) The red bars fall at the position of the geometrical shift of the edge. The accompanying overlap diagram has half-circles having the shape of each radial prism face.

Figure 11(a) shows the intensity at a distance $z = 14.3$ mm located on the maximum overlap region shown previously as the dashed red line of Fig. 8. The intensity plot along the x-axis shown in Fig. 11(b) displays how much the central fringe intensity diminishes. Observe that this central fringe is 1.75 times higher than the initial intensity, but the fringes next to it rise as high as 3.2 times higher. There is a better contrast on the first five fringes of this intensity plot. However, now that the maximum intensity is above three times the intensity of the input beam, it is possible to attribute the decrease of contrast to the small contribution coming from the wings of the Gaussian. The first three central fringes have the highest contrast, where now the points with nearly no light are closer to the optical axis compared with the previous case of Fig.10(b), and also there are two points of destructive interference near $x = \pm 130$ μm.

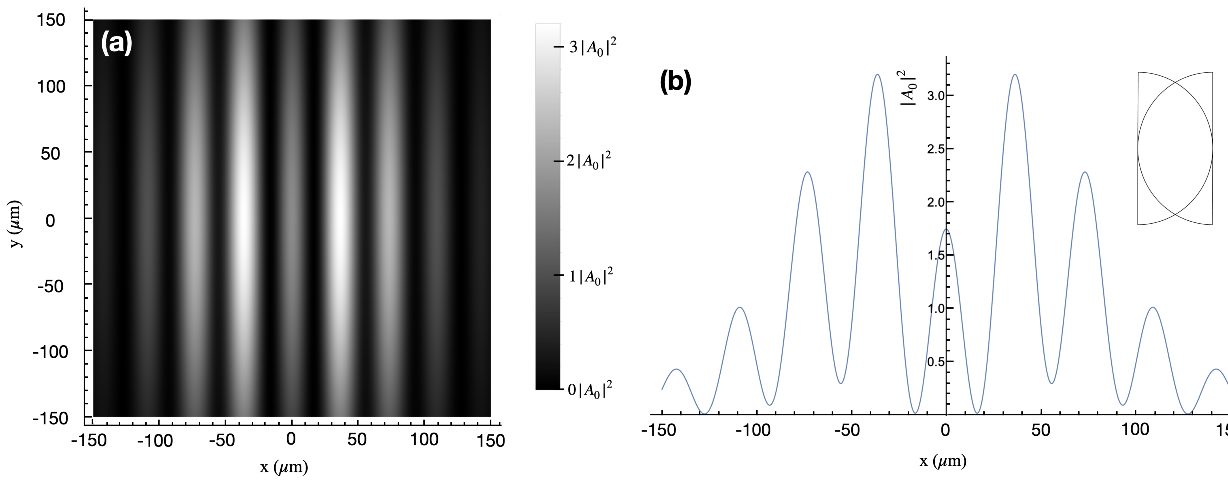

Figure 11. **(a)** Intensity in the $x - y$ plane for a biprism with $z = 14.3$ mm, $\lambda = 633$ nm, $\theta = 0.5°$, and $w = 0.25$ mm. The sidebar indicates the intensity of the fringes. Now the maximum is 3.2 times higher than the input beam and falls into the two neighbor fringes of the central one. **(b)** Intensity profile along the x-axis of (a) with The inset shows the overlap region of the two halves of the Gaussian beam.

In their work Lei, *et al.*, (2006) displays uniform fringes produced by two plane waves interfering with themselves at an angle, with this they try to simulate a Fresnel biprism. However, plane wave model predicts something different from what we see. The intensity decays as we move away from the optical axis and the intensity of the generated fringes vary depending on the observation plane.

Akhlaghi, *et. al.*, (2018) perform computations like the ones presented in this section, however they explicitly made use of an aperture on their integrals and experiments. To compare with their results, Fig. 12 displays one result taken from Fig 3.b) of Akhlaghi *et al.* (2018). Also in Fig. 12, there is an additional green curve with computations from Eq.13 using their reported parameters $z = 13$ mm, $\lambda = 632.8$ nm, $\theta = 0.35°$, and $w = 4$ mm. The inset highlights the difference of the three results.

3.2 Three-faced pyramidal prism

A three-faced pyramidal prism is an optical element with a tetrahedral shape. Using similar considerations as the previous case, Fig. 13(a) shows the variation of intensity along the optical axis. Again there is an intensity variation along the optical axis. The position of the maxima of these variations is $z = 8.1$ mm. Now Fig.13(b) displays the intensity pattern on the x-y plane at a distance $z = 8.1$ mm. Note that

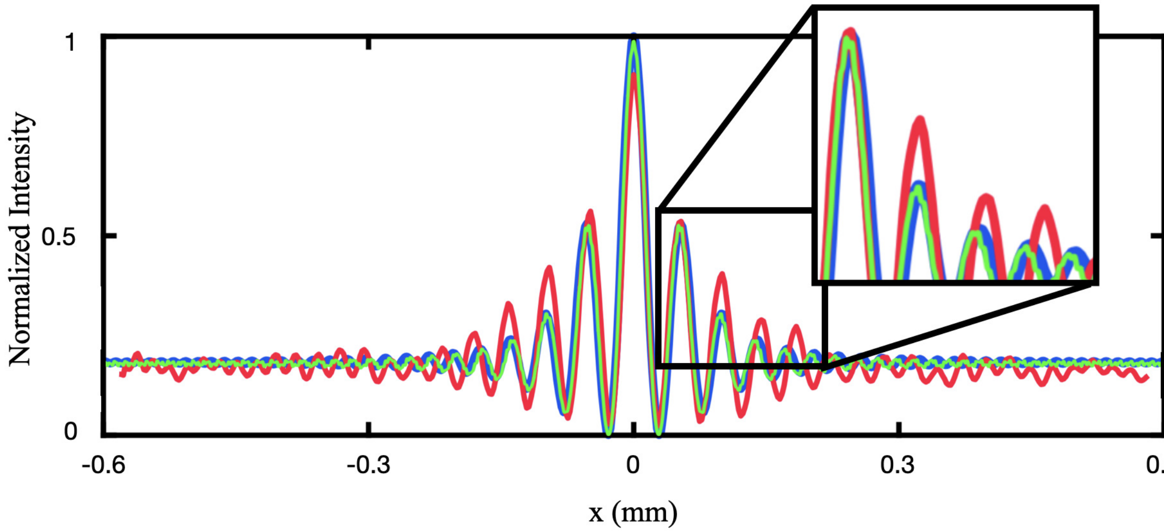

Figure 12. Intensity profile along the x-axis taken from (Akhlaghi $et\ al.$, 2018) with $z = 13$ mm, $\lambda = 632.8$ nm, $\theta = 0.35°$, and $w = 4$ mm. In red are their experimental data, blue is their computation, and green are from the theory presented in this work. The inset highlights the intensity differences.

bright spots seem to fall on the vertex of an hexagon, joined by bridges to the central spot. The central bright spot has an intensity over $13|A_0|^2$.

Figure 13(c) shows the intensity along the x-axis of Fig. 13(b). The profile shows that the nearest central spots reach up to four and six times $|A_0|^2$. There is a zero of intensity near $x = 73$ μm. The two minima at approximately $x = \pm 27\,\mu$m correspond to bridges that link the central spot and have an intensity of about $1.5|A_0|^2$. The inset shown in the figure depicts the overlap diagram, and the hexagon of the three wedges of light discussed previously represents the overlap region. Figure 13(d) illustrates the symmetry along the y-axis of Fig. 13(b). Four dark spots surround the central peak that rises above $13|A_0|^2$. The dark spots are indeed zeros of intensity located at $x = \pm 35$ μm and $x = \pm 55$ μm, and the hump rising between them are bridges that faintly connect the six spots to the central one.

Figure 14(a) shows the pattern at $z = 14.3$ mm. The well-defined spots are connected by bridges of light the brightest spots have an intensity of $7|A_0|^2$. Also, note the three dark regions with a width of approximately 30 μm next to the center spot. Fig. 14(b) displays the intensity profile along the x-axis. Despite having two bright peaks up to $6|A_0|^2$ there is a zero in intensity at approximately at $x = -27$ μm, confirming that those regions previously mentioned are points with no light. The valley between the central spot and the one to the right shows the intensity of the bridges connecting the spots.

More information can be obtained from the previous Fig.13(b). For example, Fig. 15 shows two hexagons surrounding the central spot that have at their vertices either dark or bright spots. The distance between

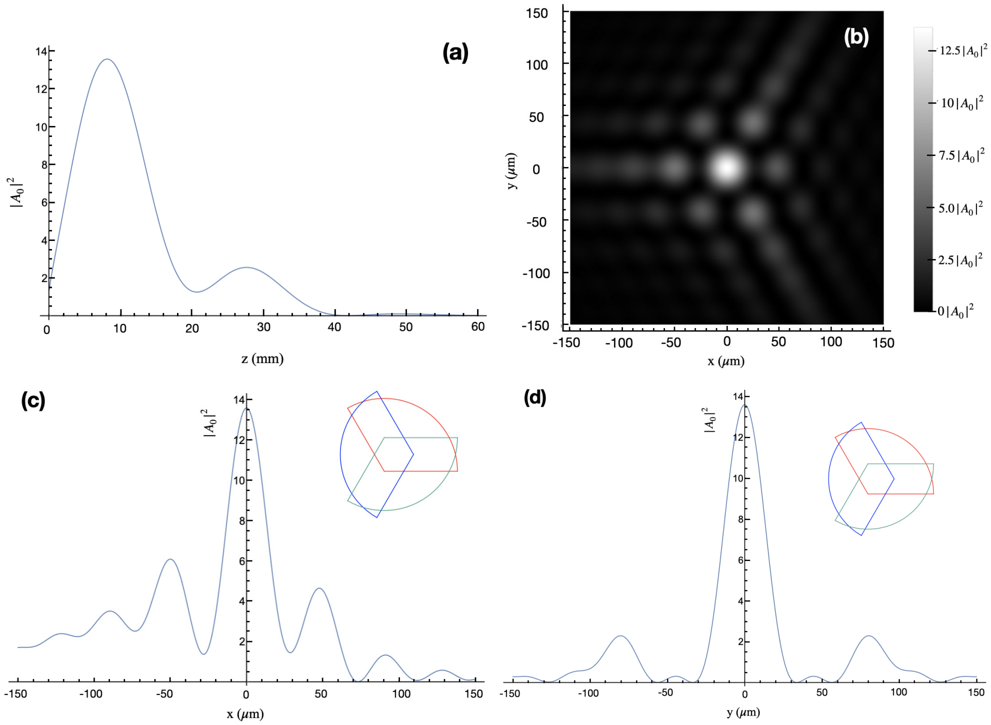

Figure 13. **(a)** Intensity along the optical for a three faced pyramid with $\lambda = 633$ nm, $\theta = 0.5°$, and $w = 0.25$ mm. The maximum is located at $z = 8.1$ mm. **(b)** Intensity in the x-y plane for a three-faced pyramid with $z = 8.1$ mm. The sidebar indicates the intensity of the fringes, where the maximum is over $13|A_0|^2$. **(c)** Intensity profile along the x-axis of (b). **(d)** Intensity profile along the y-axis of (b). The insets displays the overlap diagram of the three wedges of the Gaussian beam.

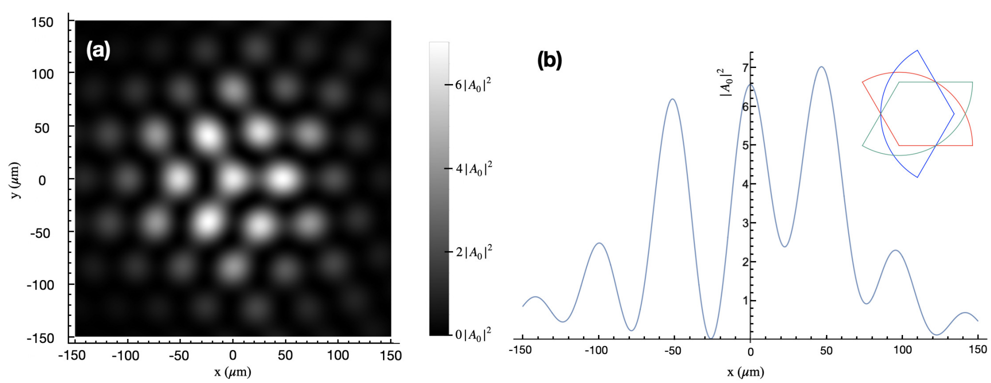

Figure 14. **(a)**Intensity in the x-y plane for a three faced pyramid with $z = 14.3$ mm, $\lambda = 633$ nm, $\theta = 0.5°$, and $w = 0.25$ mm. The sidebar indicates the intensity of the fringes, where the maximum is over seven times the intensity of the input beam. **(b)** Intensity profile along the x-axis of (a). The inset displays the overlap region of the three wedges of the Gaussian beam.

bright spots is about 50 μm from center to center and, for the dark ones, about 40 μm. A field containing bright spots is apparent, with spots faintly connected with one other; this array may find application in optical tweezers as proposed by Schonbrun, *et al.*, (2005).

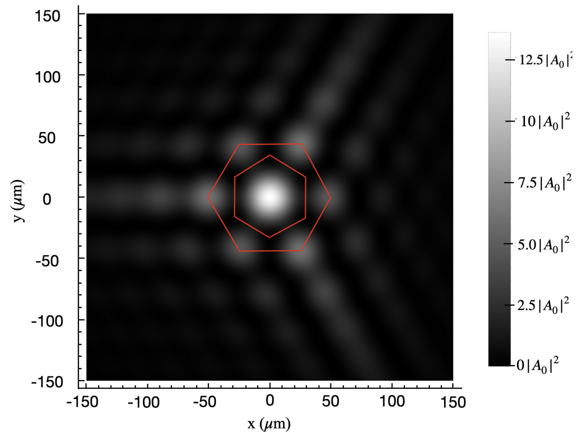

Figure 15. The intensity in the x-y plane as in Fig.13(b) where there are dark spots on the vertex of the inner hexagon and bright spots on the outer one.

3.3 Four-faced pyramidal prism

The following optical element considered is a pyramidal prism with four faces, its shape is similar to a square pyramid. The same parameters are used as before, with wavelength $\lambda = 633$ nm, refractive angle $\theta = 0.5°$, and a beam width $w = 0.25$ mm. Analyzing the intensity as it propagates at two specific distances from the prism, first at maximum intensity on the optical axis and the second near the middle of the overlap region. Plotting the intensity along the optical axis in Fig. 16(a), there is a massive increase at $z = 10.26$ mm to over $23|A_0|^2$, and then an extended shoulder with less intensity. Note compared with the previous cases now there are no apparent oscillations along the optical axis. In Chapter 5 there us a discussion this lack of intensity variations.

Figure 16(b) shows the intensity pattern in the x-y plane, at a distance $z = 10$ mm, for the four-faced pyramidal prism. It displays a central rhomboid spot. Also there are four rectangular spots closer to the central spot. These secondary spots are located at the apex of an imaginary bound square with side length 90 μm.

Figure 16(c) shows the intensity profile along the x-axis of Fig. 16(b), where the inset represents the overlap diagram for four wedges of the original Gaussian beam. This plot reveals extended regions of cancellation of light of width up to 15 μm, and besides the massive central peak, the valleys without light have a couple of peaks rising to $3|A_0|^2$.

Consider the r-axis shown in Fig. 16(d), which is the diagonal at 45° of Fig. 16(b) to see the closest spots to the central one. Here there are two points with no light at ± 21 μm. There is high contrast between the main peak and these secondary spots that rise $\approx 9|A_0|^2$. By symmetry, it is possible to obtain the same intensity pattern on the other diagonal at -45° as displayed in Fig. 16(d).

Figure 17(a) displays the intensity at a distance $z = 14.3$ mm. The pattern of light does not differ much from the previous one. However, secondary minima are higher than the ones on Fig. 16(a),, where the central spot has an intensity of almost $19|A_0|^2$, while the four spots closest to the center have an intensity $\approx 10|A_0|^2$. Figure 17(b) shows the intensity profile along the x-axis from Fig. 17(a). This plot reveals extended regions up to 15 μm with almost no light, displaying a higher contrast compared with the previous case shown in Fig. 16(c). Figure 17(c) shows the intensity of the brightest spots by plotting the intensity on the diagonal at 45° of Fig. 17(a). Here is possible to observe that the intensity of the neighboring spots is half the maximum intensity of the central spot, and the minima between them does not reach zero. The zeros of intensity are located about $r = \pm 56$ μm away from the optical axis. Overall, this case may encounter applications in optical trapping and lithography due to the high contrast of the spots and the well-defined valleys of zero intensity. This case can be a robust method to produce light spots with a fixed distance between them.

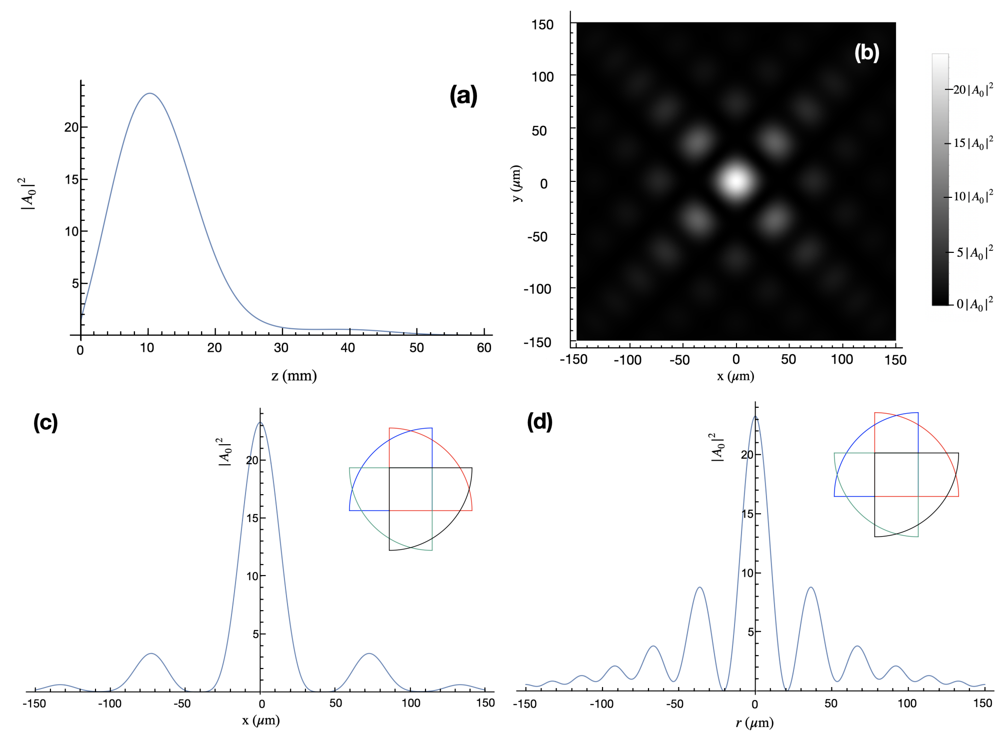

Figure 16. **(a)** Intensity along the optical axis for a four-faced pyramid with $\lambda = 633$ nm, $\theta = 0.5^\circ$, and $w = 0.25$ mm. The location of the maximum is at $z = 10.26$ mm. **(b)** Intensity in the x-y plane for a four-faced pyramid at $z = 10$ mm. **(c)** Intensity profile along the x-axis of (b). **(d)** Intensity profile along the diagonal at 45° in (b). The insets display the overlap region of the four wedges of the Gaussian beam.

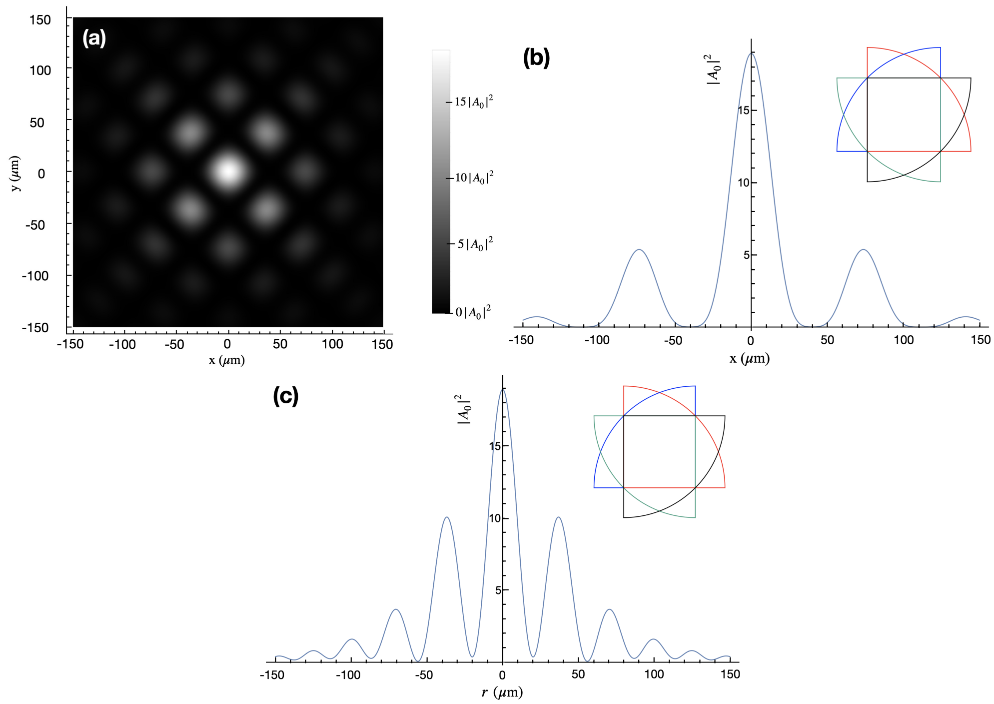

Figure 17. **(a)** Intensity in the x-y plane for a four-faced pyramid with $z = 14.3$ mm, $\lambda = 633$ nm, $\theta = 0.5°$, and $w = 0.25$ mm. The sidebar indicates the intensity of the fringes, where the maximum is almost 19 times the intensity of the input beam. **(b)** Intensity profile along the x-axis of (a). **(c)** Intensity profile along the diagonal at $45°$ in (a). The insets display the overlap region of the four wedges of the Gaussian beam.

3.4 Five-faced pyramidal prism

Now consider a pyramidal prism with five radial sides. In particular, here is presented an analysis of the intensity at two specific distances $z = 11.6$ mm and $z = 14.3$ mm. The first one corresponds to the situation when encountering a maximum in intensity on the optical axis, and the second one is near the middle of the overlap region.

Figure 18 shows the intensity along the optical axis. A single peak of intensity rises above $30|A_0|^2$ at a distance $z = 11.6$ mm. Note that there are no oscillations visible along the optical axis, in contrast with the previous cases. Figure 19(a) displays the intensity at the x-y plane, where a ring of light surrounds a central spot; however, there is low contrast between the central spot and the surrounding ring.

Figure 19(b) shows the intensity profile along the y-axis from Fig. 19(a). The intensity difference between the central spot peak and the highest point of the surrounding peaks is around $27|A_0|^2$. The inset in Fig. 19(b) is the overlap diagram with five wedges intersecting each other. The decagon at the center is where the five wedges interfere.

Figure 20(a) shows the intensity in the x-y plane at $z = 14.3$ mm. The maximum intensity rises to

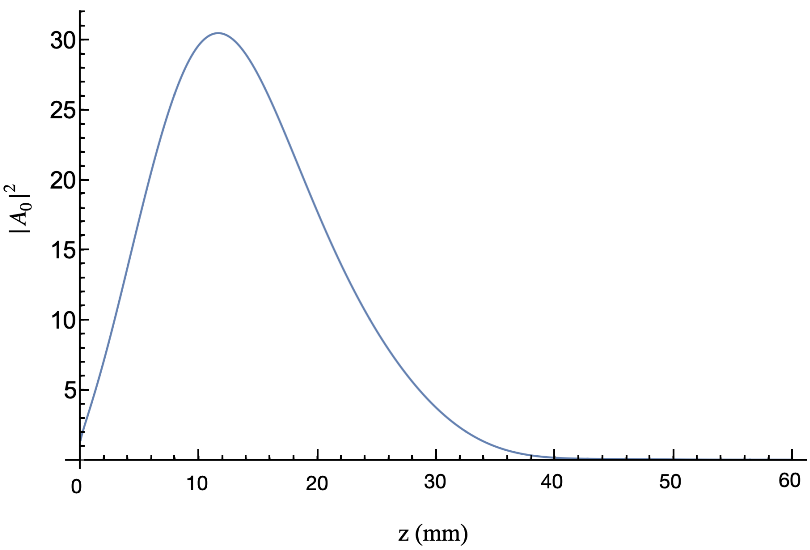

Figure 18. Intensity along the z-axis for a five faced pyramid with $\lambda = 633$ nm, $\theta = 0.5°$, and $w = 0.25$ mm. The maximum is located at $z = 11.6$ mm.

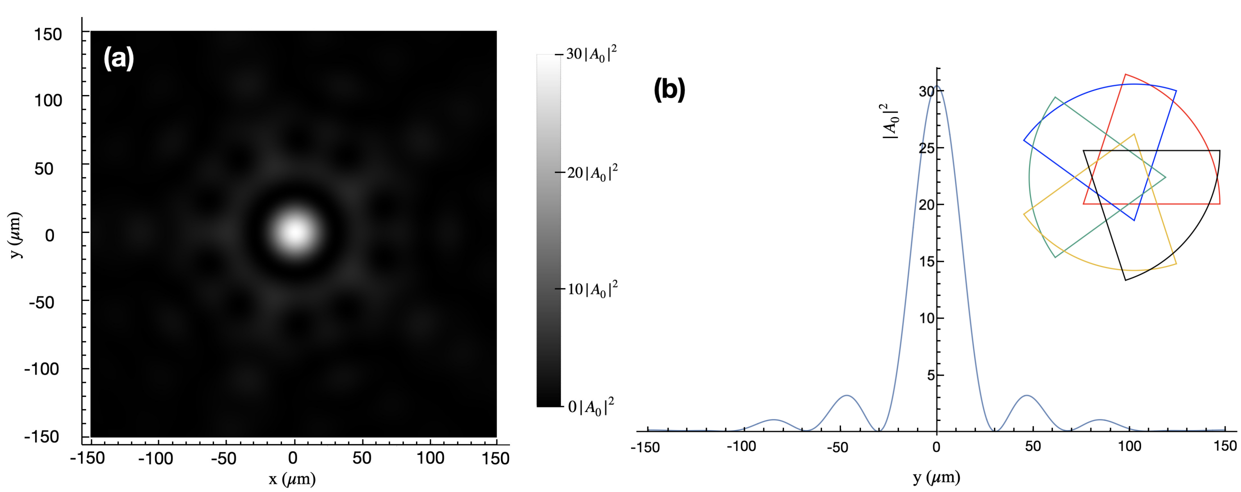

Figure 19. **(a)** Intensity in the x-y plane for a five-faced pyramid with $z = 11.6$ mm, $\lambda = 633$ nm, $\theta = 0.5°$, and $w = 0.25$ mm. The sidebar indicates the intensity of the fringes, where the maximum is over 30 times the intensity of the input beam. **(b)** Intensity profile along the y-axis of (a) The inset display the overlap region of the five wedges of the Gaussian beam.

nearly $28.5|A_0|^2$. Now there is slightly more contrast than in the previous case. In addition to the ring surrounding the central spot, ten arms of light are seen pointing from the center.

In Fig. 20(b) there is a plot of the intensity profile along the y-axis of Fig. 20. The slight increase in contrast is notable. The inset is the overlap region of five wedges where there is an increase in the overlap area between wedges.

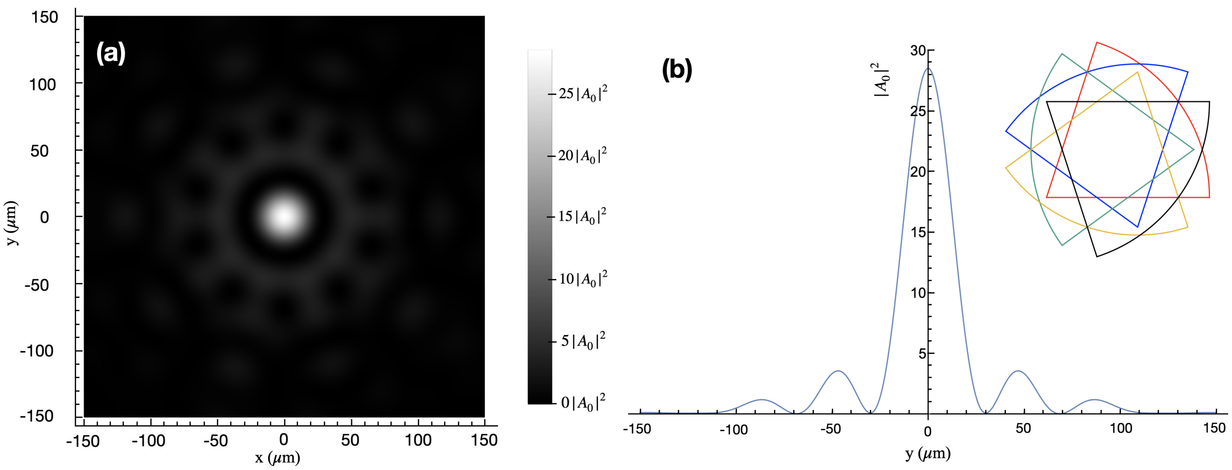

Figure 20. **(a)** Intensity in the x-y plane for a five-faced pyramid with z = 14.3 mm, λ = 633 nm, $\theta = 0.5°$, and $w = 0.25$ mm. The sidebar indicates the intensity of the fringes, where the maximum is over 28 times the intensity of the input beam. **(b)** Intensity profile along the y-axis of (a). The inset displays the overlap region of the five wedges.

3.5 Seven-faced pyramidal prism

In the case of an acute pyramidal prism with $N = 7$ as shown by Ochoa *et al.* (2021), the parameters used for the simulations are refraction angle $\theta = 2.5°$, $\lambda = 633\,\mathrm{nm}$, $w = 0.5\,\mathrm{mm}$, and $R \to \infty$. Figure. 21 shows the intensity for three different distances z. These plots are each accompanied by their corresponding overlap diagram.

For $z = 0.35\,\mathrm{mm}$, I_a exhibits a bright central spot, as well as faint lines near prism edges. The corresponding overlap diagram indicates that there is only a slight overlap at the center and along prism edges; constructive interference in these regions thus produces the features seen in I_a. The case with $z = 4.35\,\mathrm{mm}$ is quite different and exhibits a field full of interference, consistent with the corresponding overlap diagram showing the geometrical overlap of all faces throughout the region covered by the intensity plot. This case indeed presents the maximum power (32%) as a function of z within the region plotted for I_a, which may be considered optimal in this sense. Moving farther from the prism (Fig. 21(c) with $z = 8.35\,\mathrm{mm}$), I_a decreases (now 15% of power falls within the plotted region), although its general appearance does not change greatly. The corresponding overlap diagram shows that the outer parts of

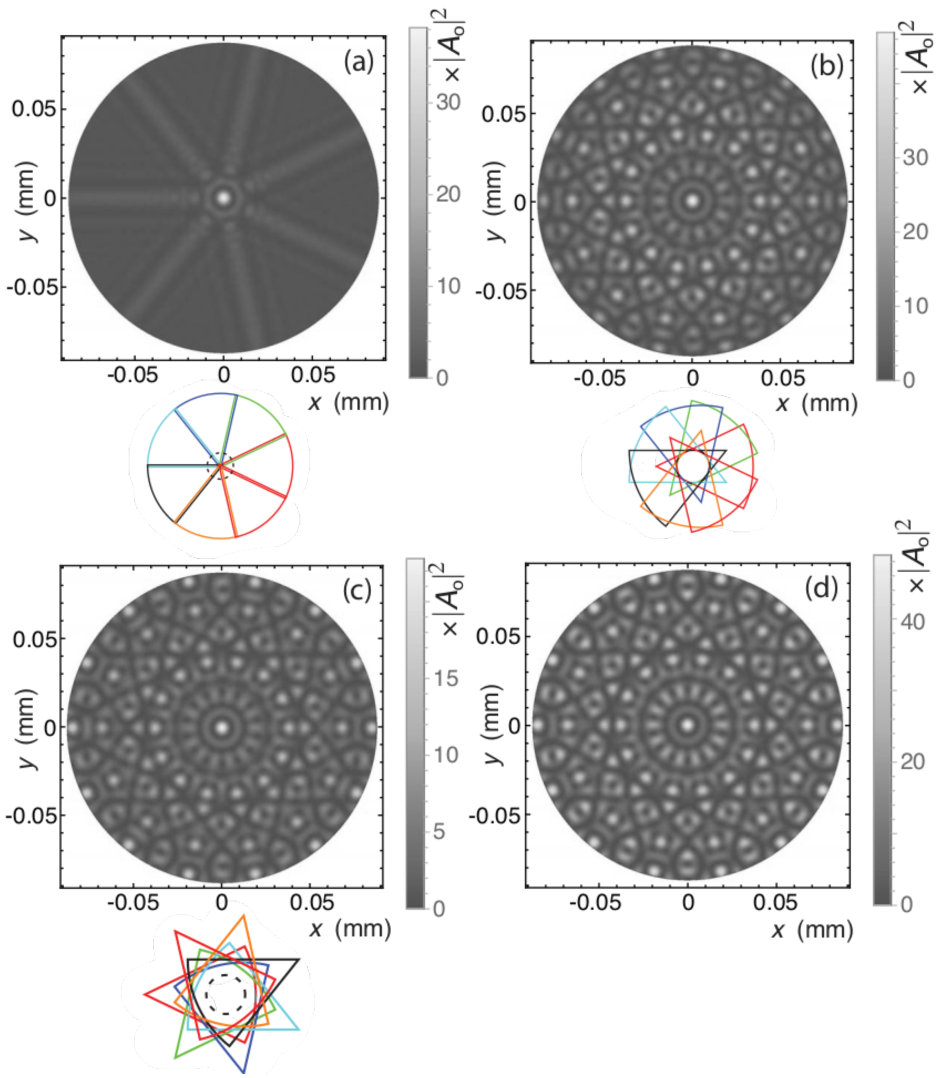

Figure 21. Intensity I_a in the x-y plane for an acute prism with 7 radial faces for propagation distances (a) $z = 0.35\,\mathrm{mm}$, (b) $z = 4.35\,\mathrm{mm}$, and (c) $z = 8.35\,\mathrm{mm}$, with associated overlap diagrams below. The case shown in (d) I_{PW} from the plane wave model of Eq. (32). Parameters are $\lambda = 633\,\mathrm{nm}$, $\theta = 2.5°$, $w = 0.5\,\mathrm{mm}$, and $R \to \infty$.

the original beam now lie near the optical axis, so it is quite reasonable that I_a has lower levels. Throughout all three cases, I_a presents the seven-fold symmetry as expected, and now interference features are $\approx 10\,\mu\mathrm{m}$ wide, of the order of $\lambda/\sin\theta$, since there is an increase of the refracting angle compared to the previous cases.

Figure 22 shows the intensity I_a in the x-z and y-z planes. The intensity in both plots appears nearly as lines in the z direction. For small z, there is a bright spot near the optical axis with little other interference, as noted earlier in Fig. 21(a). As z increases, more interference maxima appear farther from the axis as the width of the overlap region increases. For yet larger z, the broad distribution fades as the light moves away from the optical axis. I_a is symmetrical about the optical axis in the y-z plane; however, this symmetry is not present in the x-z plane, although the asymmetry in Fig. 22 is mild.

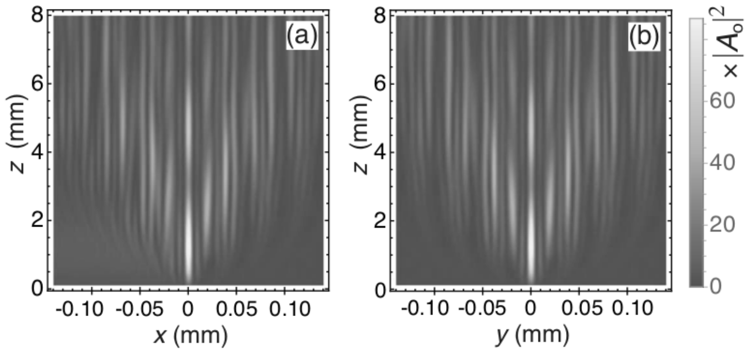

Figure 22. Intensity I_a in the (a) x-z and (b) y-z planes for an acute prism with 7 radial faces. Parameters as in Fig. 21.

To compare these results with the plane wave model, Fig. 21(d) shows a plot of $I_{PW} \equiv |A_{PW}|^2$. The qualitative comparison with the cases of Fig. 21(b)-(c) is quite good, indicating that the model here is qualitatively similar when there is good overlap. Still, the plane wave model has its clear limitations. For example, the intensity of the plane wave model is here *constant* in z; this is a consequence of the z component of $\vec{k}_n$ in Eq. (32) being identical for all N terms so that it removes the z-dependence upon taking the squared modulus. This is quite unlike the realistic diffraction calculations of Fig. 22, which shows the z-dependence of the overlap region.

3.6 Axicon limit as $N \to \infty$

In this section, a set of calculations demonstrate the numerical convergence of the Fresnel diffraction approach developed in this thesis to a well-known result. In particular, the light transmitted by an axicon will produce a Bessel beam in a region with good overlap that has an amplitude proportional to $J_0(kr\sin\theta)$, where J_0 denotes the Bessel function of zero-order McGloin and Dholakia (2005). An acute prism with N sides becomes an axicon as $N \to \infty$, so that the light transmitted by such a prism should resemble a Bessel beam for sufficiently large N. Figure 23 shows results for I_a along the x axis with N ranging from two to 50 and with other parameters held fixed at $\lambda = 543$ nm, $\theta = 0.5°$, $w = 1.0$ mm, $R \to \infty$, and $z = 50$ mm. The result with $N = 2$ is the case of a biprism that produces fringes over a wide field, which is quite different from a Bessel beam. The next case showed with $N = 7$ has a far more compact and higher distribution, where the intensity coincides with that of a Bessel beam from the central maximum through the nearest secondary maxima. With $N = 15$, this agreement extends to the nearest three secondary maxima, with the central peak continuing to increase in height. These trends continue for the case shown with $N = 50$, with good agreement with the Bessel beam seen throughout the plot. Even though no results show the full x-y plane, note that I_a for $N = 7$ shows the nearest secondary maxima as a continuous ring. At the same time, for $N = 50$, it has a total of 10 continuous secondary rings. Elsewhere, related results have been noted for plane wave model Lei *et al.* (2006).

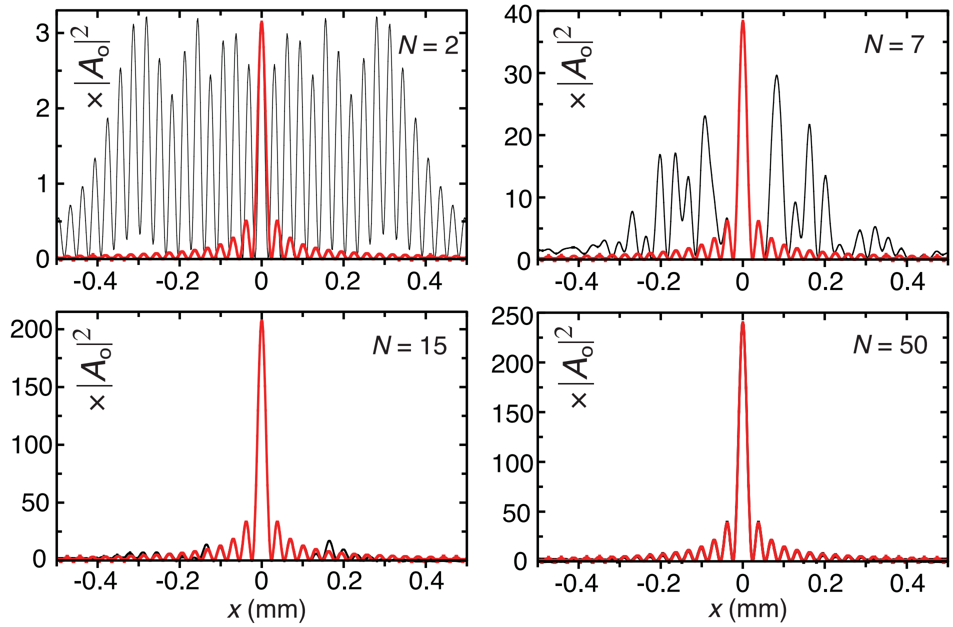

Figure 23. For the number of prism faces N as indicated, intensity I_a (black curve) along the x axis compared with the intensity of a Bessel beam (red curve) scaled to the same central height. Parameters are $\lambda = 543$ nm, $\theta = 0.5°$, $w = 1.0$ mm, $R \to \infty$, and $z = 50$mm.

The results of Fig. 23 thus further validate our method and demonstrate that it presents no difficulties for large N. The computational time required even varies a little throughout the cases shown. Because, for large N in Eq. 25, there is no increase in the net size of the integration domain.

Chapter 4. Numerical results for flat-topped pyramidal prisms

This chapter presents numerical results demonstrating typical intensity distributions for flat-topped pyramidal prisms. Starting with the simplest case of a flat-topped pyramidal prism having three radial sides, introducing some new nomenclature, and discussing the main differences between the developed model of this work against the plane wave model. Also, there are two explicit comparisons between a flat-topped pyramidal prism and an acute pyramidal prism having the same number of radial sides.

4.1 Flat-topped pyramidal prism having three radial sides

This section considers a case of a flat-topped prism having $N = 3$ radial sides with a narrower beam with $w = 0.125\,\mathrm{mm}$, while other parameters are refraction angle $\theta = 2.5°$, $\lambda = 633\,\mathrm{nm}$, and $R \to \infty$. The chosen cap width parameter is $\rho_\circ$ so that the power passing through the cap is identical to the power passing through any of the three radial sides; through numerical integration, the necessary condition is $\rho_\circ = 0.30\,w$.

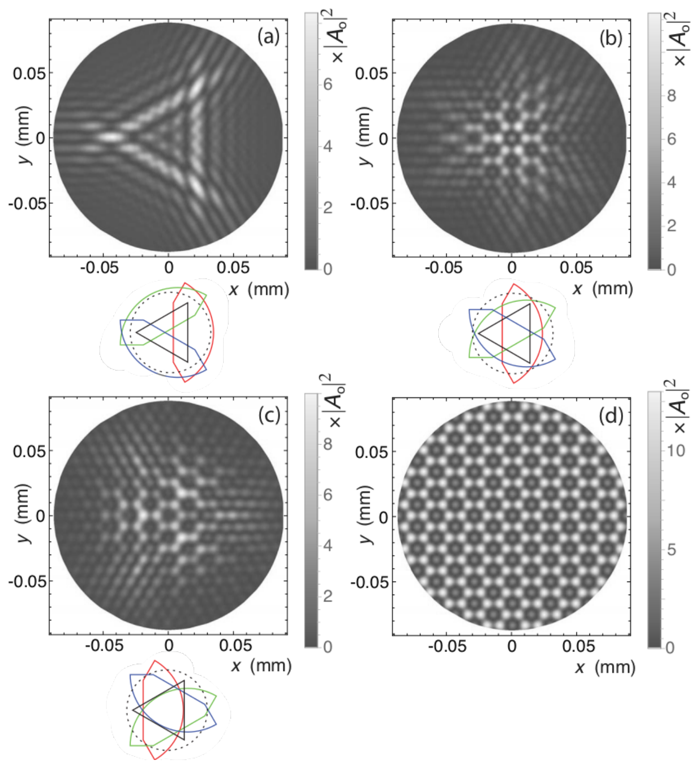

Figure 24. Intensity I_{tc} in the x-y plane for a flat-topped prism with three radial faces for propagation distances (a) $z = 0.71\,\mathrm{mm}$, (b) $z = 1.38\,\mathrm{mm}$, and (c) $z = 2.05\,\mathrm{mm}$, with associated overlap diagrams below. Also shown is (d) I_{PW} for $z = 1.38\,\mathrm{mm}$ from the plane wave model of Eq. (31). Parameters are $\lambda = 633\,\mathrm{nm}$, $\theta = 2.5°$, $w = 0.125\,\mathrm{mm}$, $R \to \infty$, $\rho_\circ = 0.30\,w$, and $\delta = k\rho_\circ \sin\theta$.

From numerical evaluation of Eq. (30) it is possible to determine $I_{tc} \equiv |A_{tc}|^2$ which is shown in Fig. 24

in the x-y plane for three evenly-spaced positions along z. The first case (Fig. 24(a), $z = 0.71\,\mathrm{mm}$) has a triangular appearance. Its corresponding overlap diagram indicates that the light from the triangular central cap overlaps along its borders with the light of the three radial faces; thus, the interference in these regions produces the triangular feature. The next case shown (Fig. 24(b), $z = 1.38\,\mathrm{mm}$) still has a somewhat triangular appearance, but near its center the intensity takes on a hexagonal form. The overlap diagram reveals that this region is where all sides contribute; no such region had been present in the previous case. In the third case shown (Fig. 24(c), $z = 2.05\,\mathrm{mm}$), the hexagonal region has spread and has become somewhat irregular. Here the overlap diagram indicates that the dimmer parts of the original beam are now crossing the propagation axis as the brighter parts move farther from the axis. Also, the region in which all sides contribute in the overlap diagram has expanded.

A complete understanding of this behavior follows from the plane wave model of Eq.(31). To evaluate the model, the phase δ of Eq.(31) associated with the prism sides must be specified. This is done by examination of $\mathcal{A}_{tc}$ of Eq. (30), where the prism side term $\mathcal{A}_{dc}$ carries the relative phase factor $e^{ik\rho_\circ \sin\theta}$. Thus the evaluation of Eq.(31) with $\delta = k\rho_\circ \sin\theta$, and the resulting plot of I_{PW} is shown in Fig. 24(d) for $z = 1.38\,\mathrm{mm}$. There it is seen that I_{PW} takes on a uniform hexagonal appearance that is similar to the central region of I_{tc} in Fig. 24(b). This indicates that, if only for a few hexagonal cells near the axis, I_{tc} has some resemblance to the plane wave model.

In Fig. 25, further comparisons are made between I_{tc} and I_{PW} in the x-z and y-z planes. The periodic appearance seen there in I_{PW} in z arises from the interference between the first wave of Eq. (32) with any of the waves within the sum; examination of the corresponding interference terms shows that the z-periodicity is given by $\Lambda_z = \lambda/(1-\cos\theta)$, or $0.67\,\mathrm{mm}$. It is also seen that, for I_{tc} in Fig. 25(a)-(b), only the central region of the plots bears much resemblance to I_{PW} from Fig. 25(c)-(d). While I_{tc} is, of course, not periodic there, some regions have cells of size and appearance comparable to I_{PW}. The general conclusion is that, while I_{tc} has some qualitative similarity to the plane wave model, the full theory developed here is necessary to obtain an accurate picture.

It is also notable that the hexagonal pattern of I_{PW} in Fig. 24(d) changes to a variety of periodic structures in the x-y plane as z is varied. However, it returns to the hexagonal form for displacements that are multiples of Λ_z. Related behavior occurs in I_{tc}, and it is possible to see similar structures for z between the three cases of I_{tc} in Fig. 24. Figures 24(a)-(c) are spaced by Λ_z, and here exhibit the hexagonal form of I_{PW} to the extent that the overlap permits.

Generally, the plane wave model has limited relevance in Figs. 24-25; only in small regions does it bear

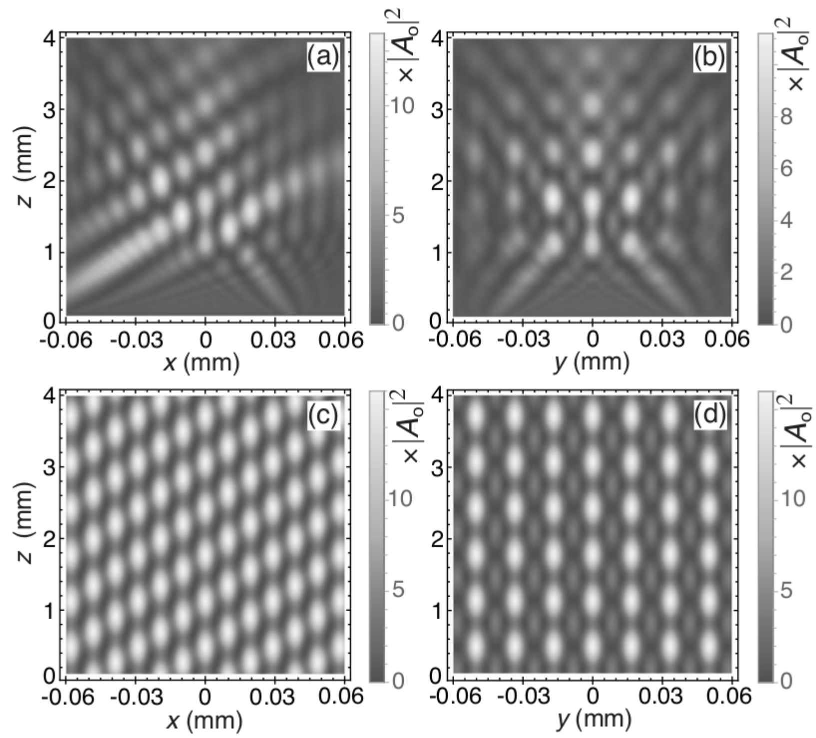

Figure 25. Intensity I_{tc} in the (a) x-z and (b) y-z planes for a flat-topped prism with 3 radial faces with parameters as in Fig. 24; corresponding results are shown in (c) and (d) for I_{PW} of the plane wave model.

similarity to the Fresnel calculations. One evident approach to obtain a result similar to the plane wave model would be to use a wider beam and a prism with a correspondingly larger parameter $\rho_{\circ}$. On the other hand, the case of Fig. 24(a)-(c) may be of interest because it is so efficient; for example, the region plotted in Fig. 24(b) contains 88% of the incident power, and even the core of the distribution (the central hexagon, and the six hexagonal cells that encircle it) contains 33% of the incident power. This high efficiency could be helpful in applications such as optical trapping or lithography. A broader point is that our approach allows us to draw such conclusions about a given configuration and change parameters until obtaining the desired behavior.

4.2 Flat-topped pyramidal prism with $N = 4$, compared with its acute analog

For the case of a flat-topped prism having $N = 4$ radial sides, here in Fig. 26 the main differences are highlighted with the corresponding acute prism. The parameters used for this case are $w = 0.125$ mm, $\lambda = 633\,\mathrm{nm}$, $\theta = 2.5°$, $R \to \infty$. The chosen cap width parameter is $\rho_{\circ}$ in order that the power passing through the cap is identical to the power passing through any of the four radial sides; the condition is met when $\rho_{\circ} = 0.297\,w$. Note that z changes on each plot by the periodicity $\Lambda_z = 0.67$ mm. The distances were selected to get similarities between all the flat-topped plots. That is each case presented here meets the periodicity criteria Λ_z of the flat-topped prism according to the plane wave model.

The intensities for an acute prism shown in Fig. 26(a) and flat-topped prism shown in Fig.26(b), both evaluated at $z = 0.71$ mm. Inspecting the case of Fig.26(a), the corresponding overlap diagram indicates that the light from the four radial faces overlaps in the center; it is the interference of these regions that produce the array of spots. Similarly, for Fig. 26(b), the corresponding overlap diagram indicates that the light from the square central cap overlaps along its borders with the light of the four radial faces; the 4-fold symmetric structure of the figure is a consequence of the interference of these regions. Besides the clear difference in the produced patterns, the maximum intensity of one point from the acute plot is nearly double the maximum reached on a flat-topped one. For the overlap diagram in Fig. 26(b), a central square represents the area of the prism cap.

Now we compare the generated patterns at a distance $z = 1.38$ mm. First, for the case of the acute prism shown in Fig. 26(c), the number of spots increases compared with Fig.26(a). They fall inside the overlap region of the four wedges of light with a decrease in the intensity of the brightest spot, interpreted as a distribution of optical power into a greater overlap region. For the flat-topped case shown in Fig.26(d), there is a contribution from the prism's faces, which produces a spotted pattern with the center brighter compared with the acute case mentioned before. Although Fig.26(c) and (d) share similarities in the position of the spots, it is the maximum intensity reached for each case that changes. Note how the brightest spots are now on the flat-topped case. From the overlap diagrams, the radial parts of light on the flat-topped case have not reached the optical axis. Hence, the central spot should not be there according to geometrical optics.

Increasing the propagation distance to $z = 2.05$ mm, now considering the interference pattern produced by an acute prism shown in Fig. 26(e) with the aid of the accompanying overlap diagram. By inspection of this plot, all the spots that fall inside a circle of radius $30\,\mu$m correspond to the overlap of all four beam parts. The distribution is broader than Fig. 26(c), and if there is an increase in the number of spots, that means less intensity on each spot. On the other hand, Fig. 26(f) displays a central bright spot surrounded by less intense spots and a faster decrease in the intensity while moving away from the center. The flat-topped corresponding overlap diagram shows that all five beam pieces interfere in this plane. Here, both plots present similarities between spot shape and location as the intensity of each spot changes.

4.3 Flat-topped pyramidal prism with $N = 7$, compared with its acute analog

The last situation considered here is a flat-topped prism having $N = 7$ radial sides and a beam width of $w = 0.5$ mm, while other parameters are the same presented in the previous section. The chosen

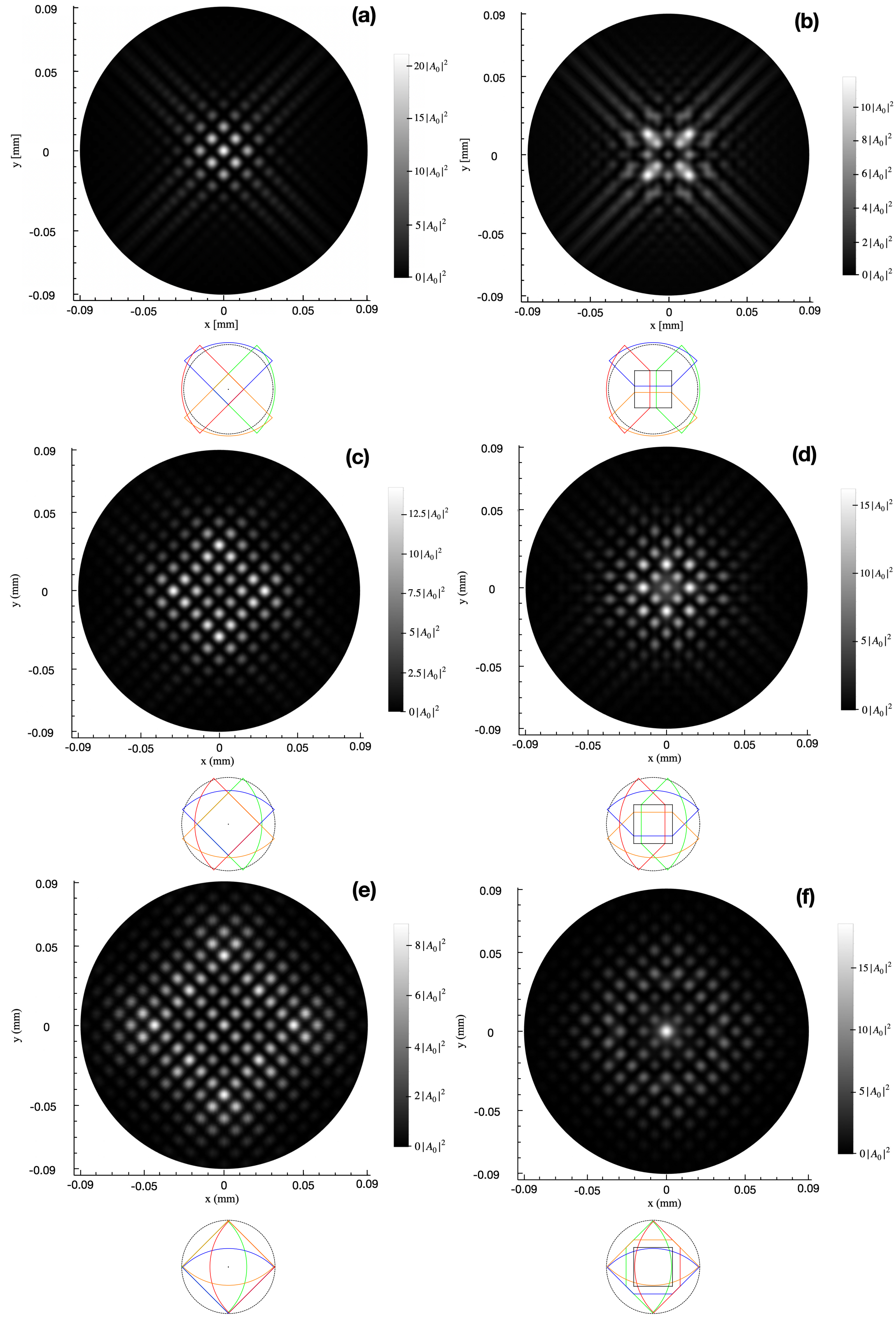

Figure 26. Intensity I_{tc} in the (a) x-y plane for an acute prism with 4 radial faces, and (b) x-y plane for a flat-topped prism with 4 radial faces at a distance $z = 0.71\,\mathrm{mm}$, (c) and (d) at $z = 1.38$ mm, and (e) and (f) at $z = 2.05$ mm. The parameters are $w = 0.125\mathrm{mm}$, $\lambda = 633\,\mathrm{nm}$, $\theta = 2.5°$, $R \to \infty$, and $\rho_\circ = 0.297\,w$.

cap width parameter is $\rho_\circ = 0.25\,w$, to meet the condition that the power passing through the cap is identical to the power passing through any of the other seven radial sides. In the following three pair of Figures 27(a)-(b), Fig. 27(c)-(d) and Fig. 27(e)-(f) is presented I_{tc} in the x-y plane for three different spaced positions along z in order to produce patterns with no matching structure for the flat-topped case. Each figure consists of results for a pair of acute and flat-topped prisms with corresponding overlap diagrams. In the case of the flat-topped overlap diagram, a black heptagon shape represents the prism's cap. Note that all the cases presented in this section do not meet the periodicity criteria. Hence there should be no resemblance between each intensity along the plane for all the flat-topped plots.

In the first pair of cases [Fig.27(a) acute and Fig.27(b) flat-topped, $z = 2.75\,\mathrm{mm}$], both patterns show no resemblance and even the maximum intensity reached by the flat-topped prism is nearly half the maximum from the acute counterpart. However, the area illuminated in the flat-top case is nearly double the area covered by the acute counterpart.

In the second case presented here [Fig.27(c) acute and Fig.27(d) flat-topped, $z = 4.75\,\mathrm{mm}$]. Note that the central spot, and the surrounding ring are similar. Further, there is a ring of a radius $50\ \mu$m consisting of 14 spots equally-spaced. At this distance, it is remarkable that the intensities are similar, as suggested by the accompanying sidebars.

In the last case [Fig.27(e) acute and Fig.27(f) Flat-topped $z = 8.75$ mm], the only noticeable similarity between plots is the central spot, but even the intensity of this spot in the acute case is dimmer than the flat-topped one.

In closing, as the number of faces increases, the resemblance between patterns acute and flat-topped decreases. Also, there may be points where some spots have the same intensity.

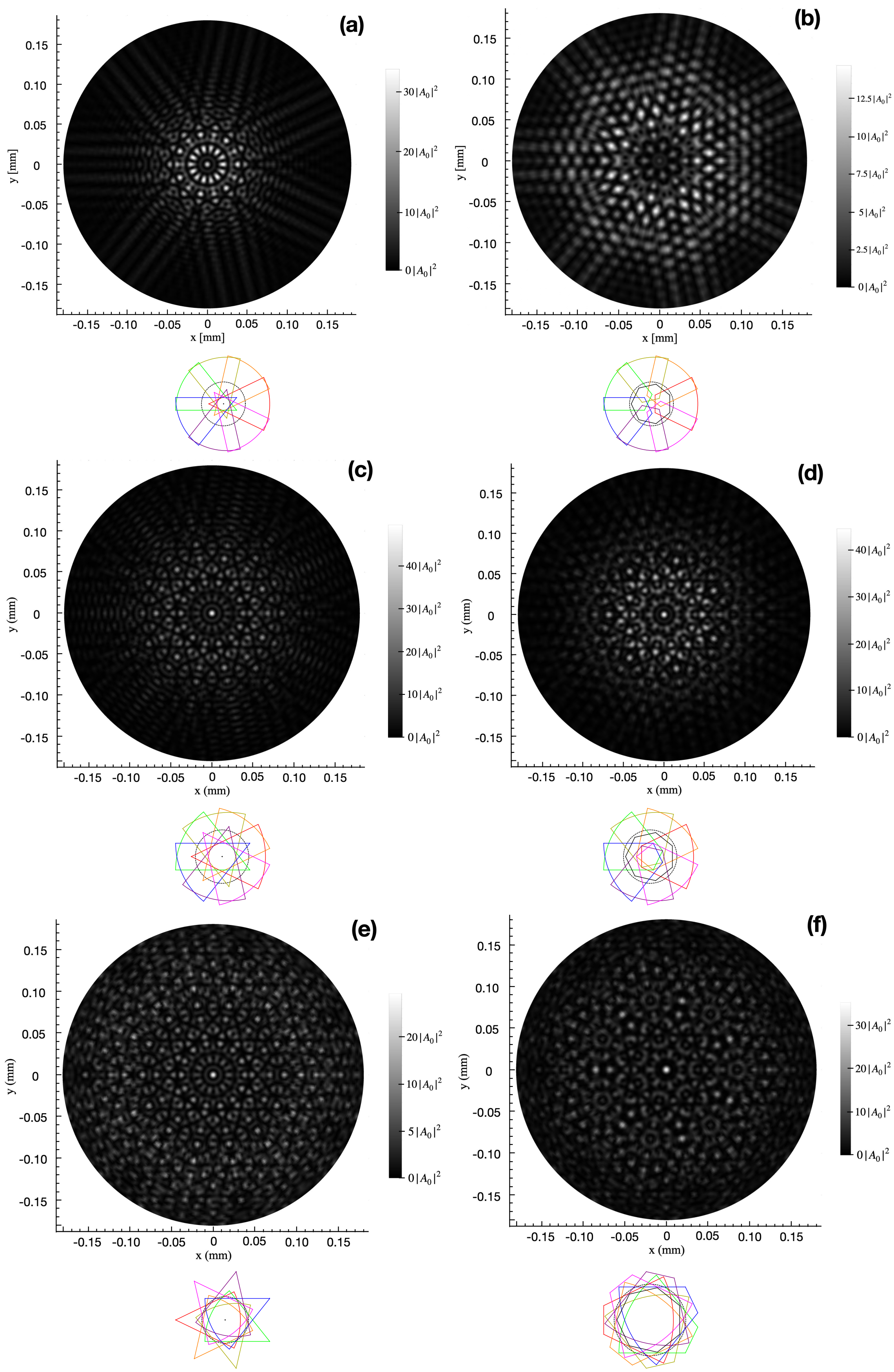

Figure 27. Intensity I_{tc} in the (a) x-y plane for a flat-topped prism with 7 radial faces at $z = 2.75\,$mm, and (b) x-y plane for a corresponding acute prism. (c) and (d) at $z = 4.75\,$mm, (e) and (f) at a distance $z = 8.75\,$mm. Parameters used are $w = 0.5$mm, $\lambda = 633\,$nm, $\theta = 2.5^\circ$, $R \to \infty$, and $\rho_\circ = 0.25\,w$.

Chapter 5. Axial intensity variation

The intensity produced by a pyramidal prism often contains oscillations along the optical axis. This chapter considers the physical origins of the oscillations and presents computed examples. Consider the case of a Fresnel biprism. Blocking one face of the prism produces a pattern of edge diffraction, which propagates at an angle θ towards the optical axis. Fig. 28 shows such a case (red curve) where the edge diffraction pattern has shifted $z\tan\theta$ or ≈ 150 μm to the left. Blocking the other side produces the same effect but reversed, as shown in the black curve of Fig. 28. Of course, with both halves of the prism uncovered, the amplitudes interfere in the plane of Fig.28. Because of physical symmetry, the two amplitudes at $x = 0$ are identical and thus interfere constructively, producing a peak. Thus as the propagation distance increases, further oscillations appear as these edge diffraction patterns shift transversely.

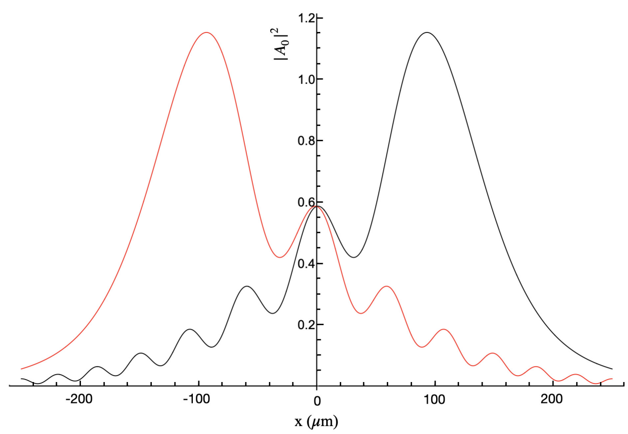

Figure 28. Intensity profile along the x-axis of biprism with $z = 23$ mm, $\lambda = 543$ nm, $\theta = 0.46°$, $R = 850$ mm, and $w = 0.25$ mm. The red and black curves correspond to the contribution from each side of the biprism.

5.1 Dependence on the number of faces

It is notable that for $N \geq 2$, related intensity oscillations appear along the optical axis. In particular, each wedge-shaped prism face produces edge diffraction; when adding the contribution from all faces, the effect produces oscillations along the optical axis. Figure 29 compares the variation along the optical axis for six prisms, one prism per curve, which share the same parameters but have a different number of faces. As seen from the figure, each peak arises from the constructive interference of the amplitudes produced by the edge diffraction contribution of each prism side. As the number of faces increases, the first intensity peak falls further down the propagation axis but with higher intensity. However, the number of oscillations diminishes and becomes broader.

Although not shown here, the limiting case as $N \to \infty$ corresponds to an axicon; its corresponding axial intensity presents only a single peak without further oscillation.

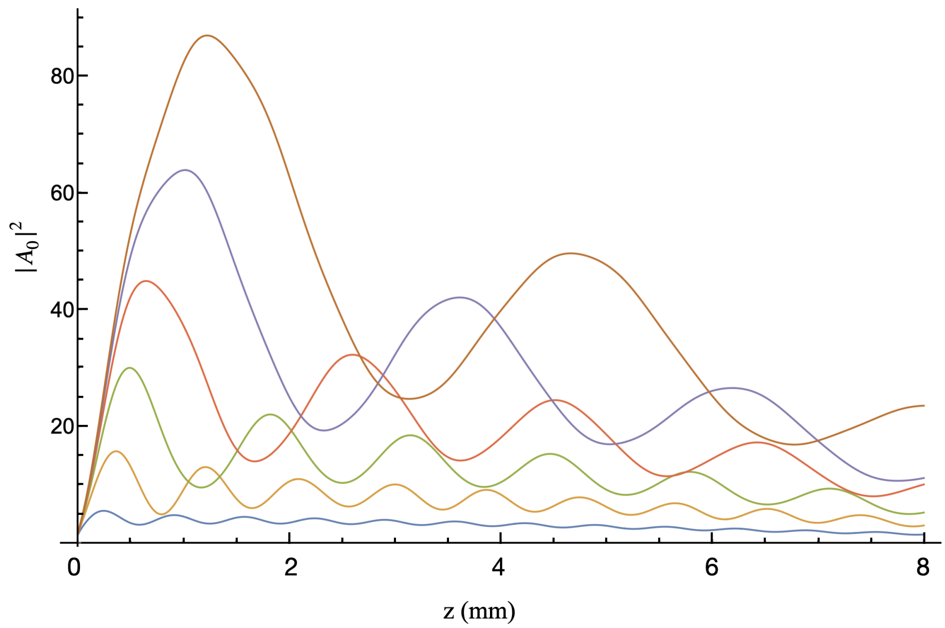

Figure 29. Intensity profile along the optical axis with $\lambda = 633$ nm, $\theta = 2.5°$, $R \to \infty$, and $w = 0.5$ mm. The curves correspond to $N = 2$ (blue), $N = 3$ (yellow), $N = 4$ (green), $N = 5$ (red), $N = 6$ (purple), and $N = 7$ (orange).

5.2 Dependence on the beam width

The beam width is another parameter that influences the intensity oscillations along the optical axis. Narrower beams produce a faster decay, and thus fewer apparent oscillations as shown in Fig.30. Note that as w increases, there is not a noticeable shift of the first maxima compared with the previous case shown in Fig. 29. Also, note how the maximum intensity reached is $\approx 30|A_0|^2$, and all the peaks fall near the same position along the axis.

5.3 Dependence on the refractive angle

The prism refractive angle θ also affects the intensity oscillations along the optical axis. Fixing all the parameters to $N = 4$, $\lambda = 633$ nm, $w = 0.5$ mm, $R \to \infty$. Note that as θ decreases the number of oscillations also decreases. Hence, a decrease in this refractive angle parameter produces broad oscillations, as shown in Fig. 31. Also, note that as there is an increase of the angle, the peaks become narrower but with slightly higher amplitude and shift near the prism apex (origin of the plot). This case uses the same parameters as the previous section, only varying the refractive angle, and the maximum amplitude reached is again $30|A_0|^2$.

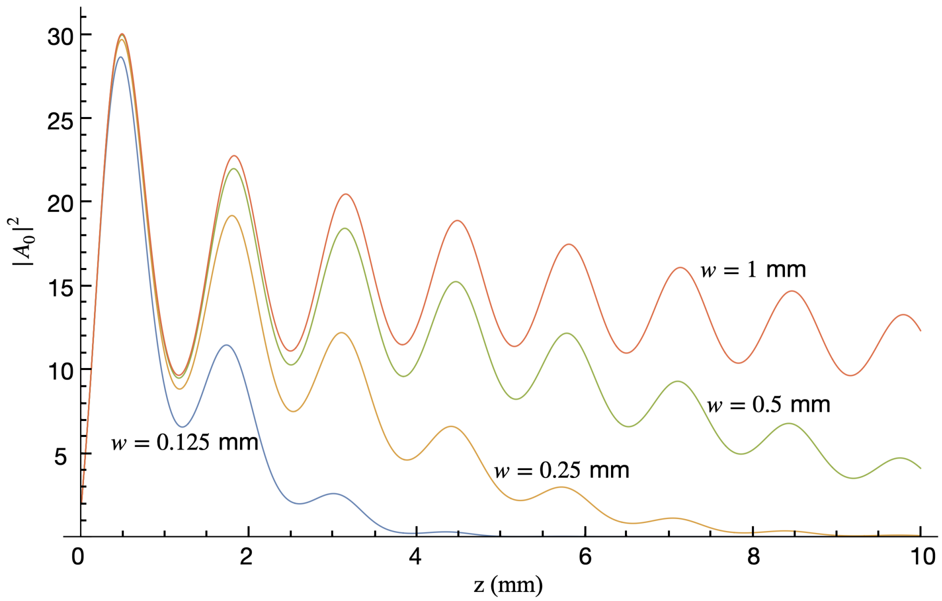

Figure 30. Intensity profile along the optical axis for different beam width w with $N = 4$, $\lambda = 633$ nm, $\theta = 2.5°$, $R \to \infty$. The values for the w parameter are attached to the corresponding plot.

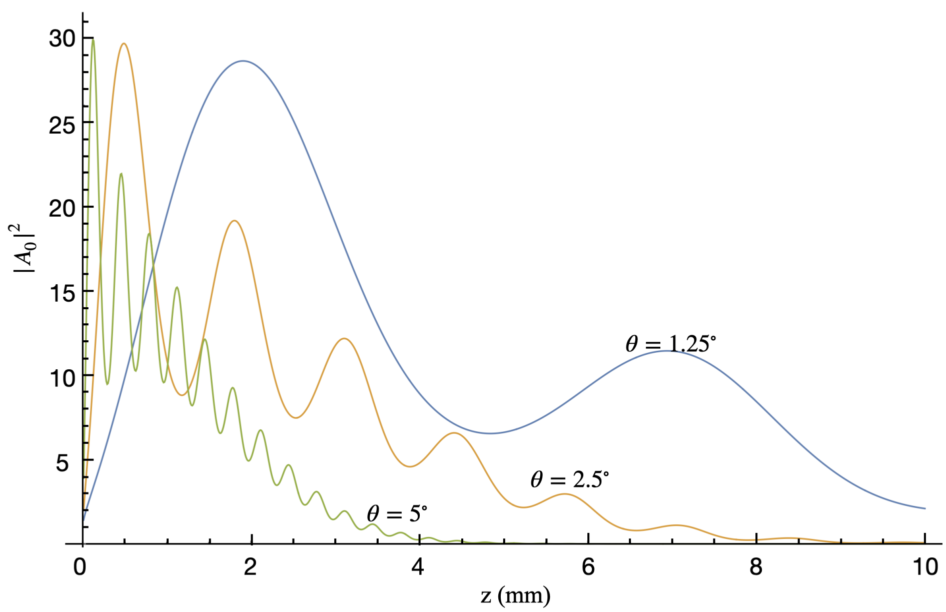

Figure 31. Intensity profile along the optical axis for different diffracted angle θ with $N = 4$, $\lambda = 633$ nm, $R \to \infty$, and $w = 0.5$ mm.

5.4 Intensity oscillations produced by a flat-topped prism

Section 4.1 presents a discussion how the plane wave model produces intensity oscillations with z-periodicity, given by $\Lambda_z = \lambda/(1-\cos\theta)$. The current section presents the related effects in this thesis calculations for a flat-topped prism. Figure 32 shows the axial intensity produced by a seven-sided flat-topped pyramidal prism with its acute prism equivalent. The acute case (yellow) shows broad oscillations while the flat-topped (blue) shows the expected oscillations Λ_z. However, note how the oscillations after a point where all the faces cross the optical axis keep oscillating but now follow the same trend as the acute prism. For the first $2\,\mathrm{mm}$, the intensity remains nearly $|A_0|^2$, then rises as soon as the diffraction contributions from the sides reach the optical axis.

For future applications, the trend followed by the flat-topped intensity may be helpful to have in mind when preparing to tailor the behavior of structured light along the axis.

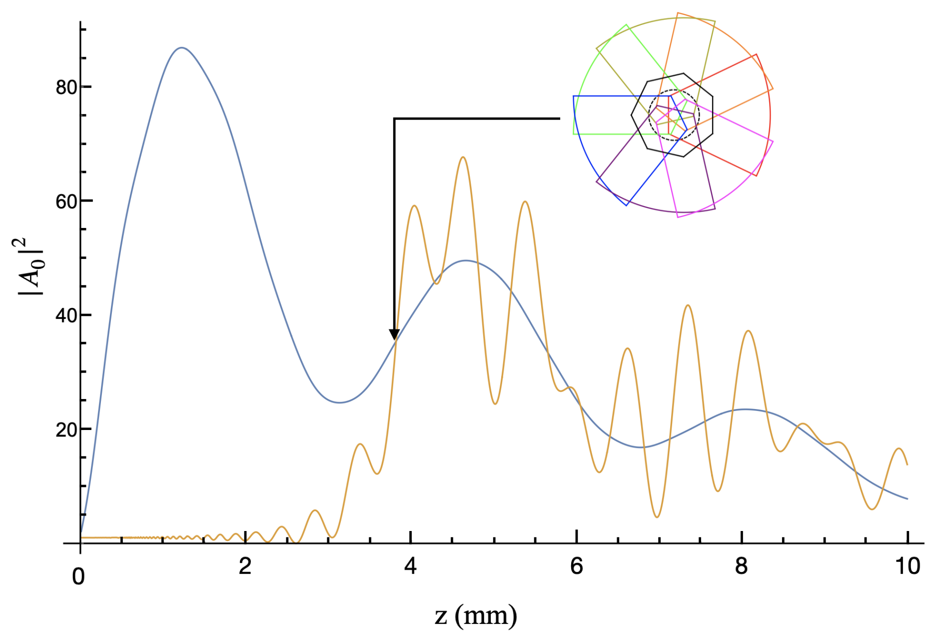

Figure 32. Intensity profile along the optical axis for an acute prism (blue), and flat-topped prism (yellow) with $N = 7$, $\lambda = 633$ nm, $\theta = 2.5°$, $R \to \infty$, and $w = 0.5$ mm.

Chapter 6. Optimized spot distributions

The following is a discussion of two cases of using a prism to efficiently generate a spatial distribution of spots with nearly identical power. Efficiency is a significant concern in optical trapping since the light modulators commonly used produce absorption, unused diffracted orders, as well as scattering from their pixels. Monolithic prisms, of course, have none of these limitations.

The cases described here were hand-picked by surveying the patterns created under various conditions and then numerically optimizing the uniformity of the spots in a few particular cases. The optimization process is varying z and w, with other parameters fixed, since the dependence on z and w was considerably stronger than other parameters, as hinted from the previous Chapter 5. Further, there is a discussion on how the patterns produced can be widely scaled in size, as desired, by varying the relative values of z, w, and θ. This scaling allows considerable flexibility in designing systems for applications such as optical trapping or lithography.

6.1 Spots with similar intensity

Consider first Fig. 33, which shows the intensity distribution I_a produced by an acute prism having $N=6$ sides, with $\lambda = 543\,\mathrm{nm}$, $w = 0.21\,\mathrm{mm}$, $\theta = 1.0°$, $z = 9.0\,\mathrm{mm}$, and $R \to \infty$. The distribution contains a total of 13 bright spots in a field containing 89% of the incident power, which include a central spot, six in a ring of average radius $0.036\,\mathrm{mm}$, and six more in a ring of average radius $0.062\,\mathrm{mm}$. All spots have similar intensity, and the inner and outer rings containing the spots each carry 25% of the incident power. The spots of such a pattern could be used for the optical trapping of several particles simultaneously, as has been done in other works (Otte and Denz, 2020; Yang *et al.*, 2021). Figure 33 also shows I_{PW} from the plane wave model of Eq. (32), which shows a periodic distribution of spots that resemble I_a, although it is clear that for I_a the finite beam only allows 13 of the spots to have high brightness.

Another case is shown in Fig. 34, which shows I_a produced by an acute prism having $N=4$ sides, with $\lambda=543\,\mathrm{nm}$, $w=0.15\,\mathrm{mm}$, $\theta=1.0°$, $z_0=6.9\,\mathrm{mm}$, and $R\to\infty$. About $0.045\,\mathrm{mm}$ diagonally from the plot center, four bright spots appear in each quadrant. The entire field plotted again contains 89% of the incident power, while the total power contained in the four distributions of four spots is 45% of incident power; thus, the creation of the spots is efficient, and again I_a shows potential for optical trapping. Figure 34 also shows the corresponding I_{PW} which shows a periodic structure of similar spots, and it becomes apparent that the finite beam producing I_a again only allows some of these spots to appear with significant brightness for the parameters chosen.

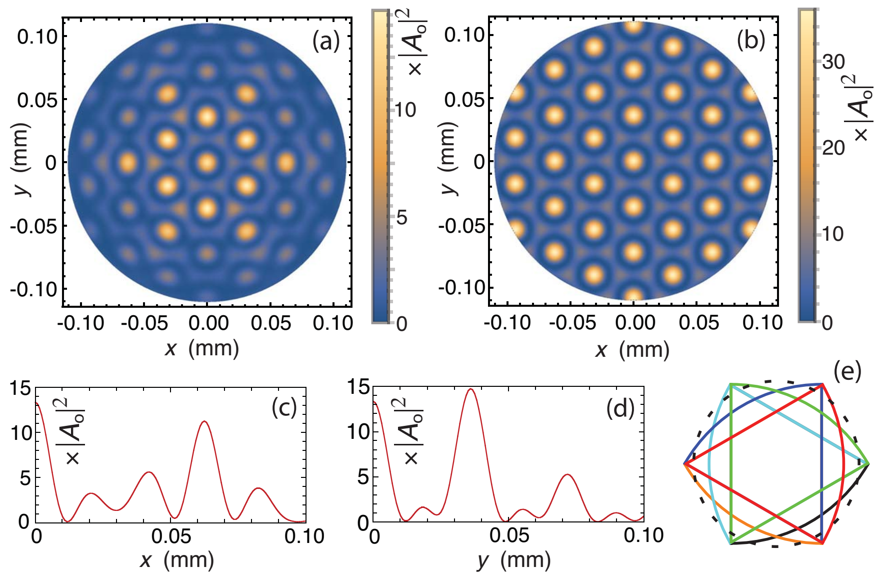

Figure 33. (a) Intensity I_a in the x-y plane for an acute prism with 6 faces, optimized to produce 13 spots of similar intensity (center, and 2 rings of 6 spots each), compared with (b) I_{PW} from the plane wave model. Also shown is (c) I_a along the x-axis, (d) I_a along the y-axis, and (e) the overlap diagram. Parameters are $\lambda = 543\,\mathrm{nm}$, $\theta = 1.0°$, $w = 0.21\,\mathrm{mm}$, $R \to \infty$, and $z = 9.0\,\mathrm{mm}$.

6.2 Scaling patterns

Note that for results as in Figs. 33-34, it is possible to scale them in their dimensions by changing parameters in a particular way. Specifically, if there is a need to scale the size of the distribution by a factor M, this may be achieved by transforming parameters as $(w, \theta, z) \to (w \times M, \theta/M, z \times M^2)$ for small θ. This transformation produces only an overall magnification M of the overlap diagram, without any changes in the relative overlap. This geometrical similarity of a transformed case implies that the new x-y intensity distribution will resemble the original magnified by M; the only exceptions so far noted are cases where strong diffraction effects arise (i.e., small prism faces, long propagation lengths).

Figure 35 shows two examples of such transformations, where the case from Fig. 33(a) has been scaled with $M = 10$, and the case from Fig. 34(a) has been scaled with $M = 1/10$. Apart from the expected width changes, there is little difference between the cases before and after scaling. Even the power percentages in analogous regions remain within 1% of the values quoted earlier. These results thus demonstrate that scaling provides a useful means of producing a pattern having a desired physical size. Note that scaling implies that intensity plots in the x-z and y-z planes are invariant if the x or y coordinates are scaled by M and the z coordinates are scaled by M^2, which implies relative compression ($M < 1$) or stretching ($M > 1$) of the overall plot along z.

Finally, in addition to scaling, note that the pattern produced by any prism is possible to be magnified or demagnified as desired by imaging with an appropriate lens. Thus there is considerable flexibility in methods to change the size of patterns like those shown here.

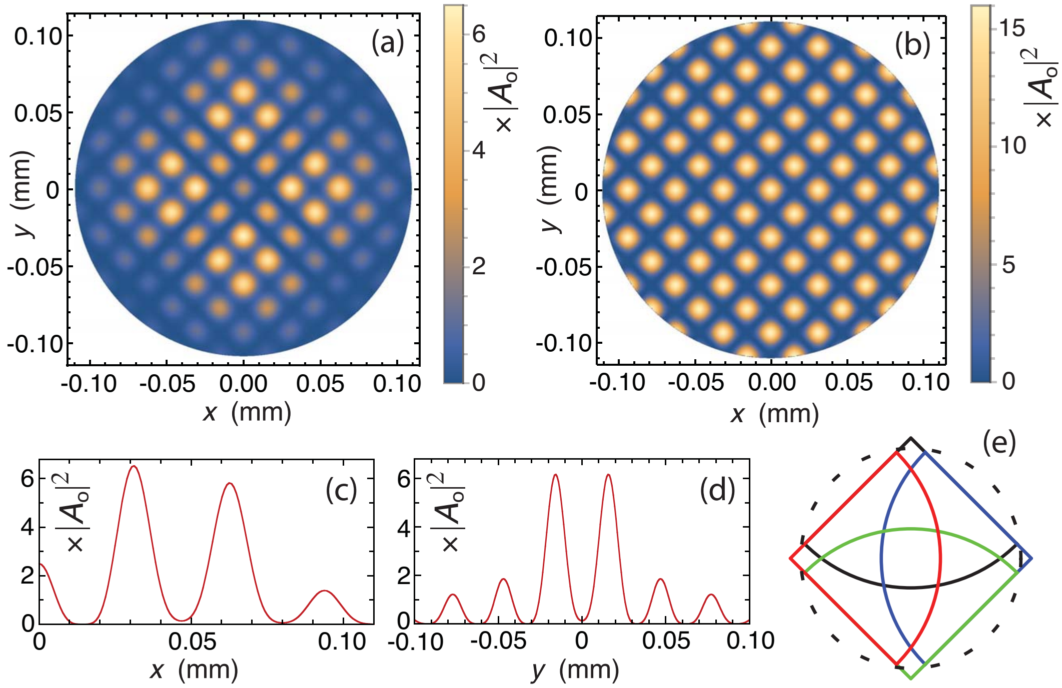

Figure 34. (a) Intensity I_a in the x-y plane for an acute prism with 4 faces, optimized to produce 16 spots of similar intensity (see 4 blocks of 4 spots), compared with (b) I_{PW} from the plane wave model. Also shown is (c) I_a along the x-axis, (d) I_a as a function of y with $x = 0.047\,\mathrm{mm}$, showing two of the bright spots, and (e) the overlap diagram. Parameters are $\lambda = 543\,\mathrm{nm}$, $\theta = 1.0°$, $w = 0.15\,\mathrm{mm}$, $R \to \infty$, and $z = 6.9\,\mathrm{mm}$.

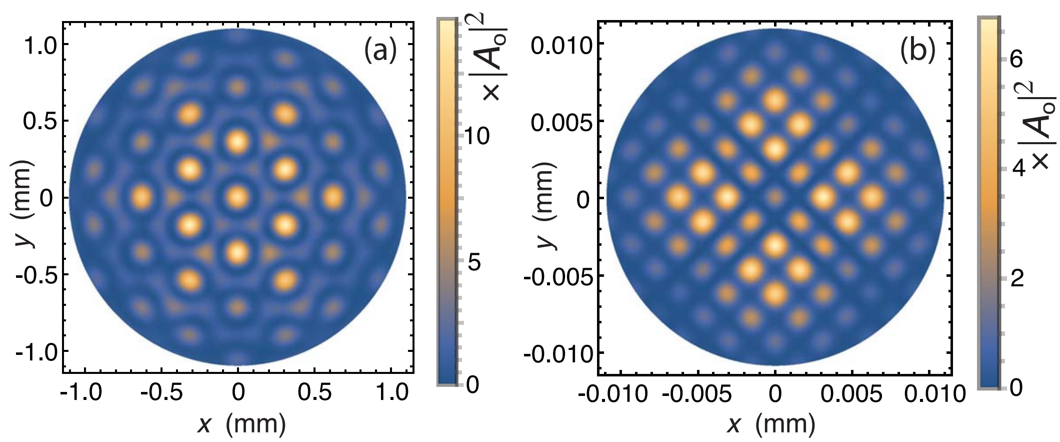

Figure 35. (a) Intensity I_a in the x-y plane obtained by scaling the parameters of Fig. 33(a) by the factor $M = 10$, and (b) I_a obtained by scaling the parameters of Fig. 34(a) by the factor $M = 1/10$.

Chapter 7. Patterns having spatial uniformity

The current chapter presents calculations showing the production of interference patterns having uniform brightness. Such cases require a broad illuminating beam covering large areas on prism faces. Consider two cases employing a four-faced acute prism; the first uses a Gaussian beam, while the second employs a higher-order mode and so requires an extension of the theory of Chapter 2. The patterns created could have applications in lithography and photonic crystal development (Wu *et al.*, 2005; Pang *et al.*, 2006; Juodkazis *et al.*, 2009; Park and Yang, 2013; Jeon *et al.*, 2018).

7.1 Gaussian beam

Results for I_a are shown in Fig. 36 for an acute prism with 4 faces, with parameters set to $\lambda = 633\,\mathrm{nm}$, $w = 5.0\,\mathrm{mm}$, $\theta = 0.5°$, $z = 260\,\mathrm{mm}$, and $R \to \infty$. The value of z was chosen with care to optimize the interference contrast of I_a. The prism cuts the incident beam into four parts that overlap in a square region that is clear in both I_a and in the overlap diagram of Fig. 36. The diagonal width of this region is $2z\tan\theta$ or $4.5\,\mathrm{mm}$, and 75% of the incident power falls within the plot boundaries of Fig. 36(a). In the overlap region (Fig. 36(b)), the spots observed are evenly spaced and resemble the periodic I_{PW} from the plane wave model, although not shown I_{PW} here. However, unlike the plane wave model, in Fig. 36 I_a exhibits some modulation in the interference envelope that arises from diffraction from prism edges. This edge diffraction is inescapable under these conditions, and whether the pattern modulation present in Fig. 36 is acceptable would depend on the particular application. In lithography, for example, the nonlinearity of the media response often used could make such mild variations inconsequential.

7.2 Hermite-Gauss mode HG_{11}

On the other hand, it is possible to produce similar patterns without significant edge diffraction effects if the illuminating beam is in a spatial mode having zeroes along prism edges. A simple case would be to use a mode with N lobes illuminating an acute prism with N faces; here is presented one such example. In particular, consider a 4-faced prism-like that used in Fig. 36, and only change the incident mode to a Hermite Gaussian HG_{11} spatial mode, oriented so that its zeroes of amplitude (midway between the modal lobes) lie along the four prism edges. Returning to theoretical development like that of Chapter 2

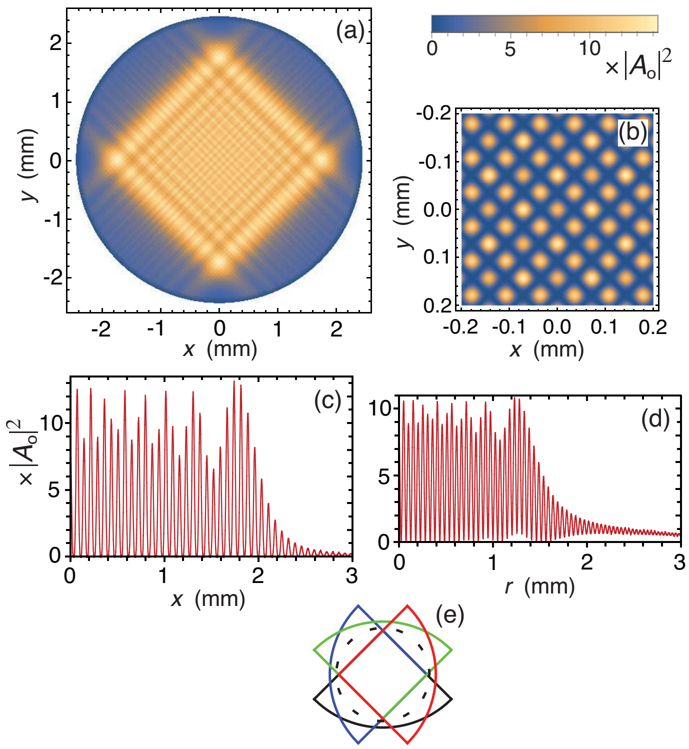

Figure 36. Results for a Gaussian mode illuminating an acute prism with four faces. Shown are (a) the envelope of the interference maxima of I_a, (b) I_a showing the interference pattern over a small region, (c) I_a along the x-axis, (d) I_a along an axis at 45°, and (e) the overlap diagram. Parameters are $\lambda = 633\,\mathrm{nm}$, $w = 5.0\,\mathrm{mm}$, $\theta = 0.5^\circ$, $z = 260\,\mathrm{mm}$, and $R \to \infty$.

and, after a similar analysis, found that Eq. (1) is valid for an HG_{11} mode if $H[\cdot]$ is there replaced by

$$\begin{aligned}
&H'[r, \phi + (n-1)\Delta\phi, \varphi, 0, \theta] = \\
&\quad (-1)^{n+1} \left[\frac{4A_0 k w^2 z^3}{\pi \alpha_1^{7/2}}\right] e^{ikr^2/(2z)} e^{-k^2 w^2 \beta_1^2/\alpha_1} \cos(2\varphi) \times \\
&\quad \Big\{ \sqrt{\pi} k w \beta_1 (3\alpha_1 + 2\gamma_1^2)[\operatorname{erf}(\gamma_1/\sqrt{\alpha_1}) - 1] - \\
&\qquad 2i\sqrt{\alpha_1}(\alpha_1 + \gamma_1^2)\, e^{-\gamma_1^2/\alpha_1} \Big\}. \qquad (33)
\end{aligned}$$

Figure 37 shows results for I_a for the HG_{11} mode with parameters as in Fig. 36, except that $z = w\tan\theta$ or $573\,\mathrm{mm}$. This distance is chosen because it provides good geometrical overlap and excellent interference contrast throughout the full pattern. In Fig. 37 it is seen that there is a broad distribution having a Gaussian-like envelope that nearly has rotational symmetry about the propagation axis. The envelope has a full width at half maximum of $4.1\,\mathrm{mm}$, which contains 53% of the incident power. The interference pattern is similar to that of Fig. 36, with one notable difference: the origin of Fig. 37 is a minimum of interference, while it had been a bright spot in Fig. 36. This difference arises because two lobes of the HG_{11} mode are 180° out of phase with respect to the other two lobes; the origin of Fig. 37 must then have zero amplitude by symmetry, and the bright spots throughout the field appear at shifted positions when compared to Fig. 36. However, it is quite clear that no edge diffraction is apparent in Fig. 37, which is the desired result.

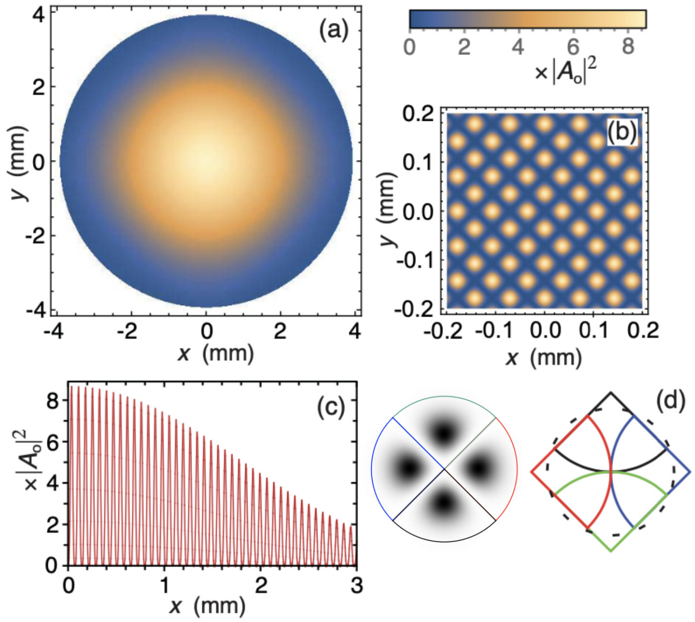

Figure 37. Results for an HG_{11} mode illuminating an acute prism with four faces. Shown are (a) the envelope of the interference maxima, (b) I_a showing the interference pattern over a small region, (c) I_a along the x-axis, and (d) the overlap diagram. Parameters are $\lambda = 633\,\mathrm{nm}$, $w = 5.0\,\mathrm{mm}$, $\theta = 0.5°$, $z = 573\,\mathrm{mm}$, and $R \to \infty$.

Figure 38 shows the intensity profile along the x-axis for three different distances from the pyramidal prism. They all share the same fringe periodicity, the overlap diagrams show the parts of the beam interfering at each distance. Each one of the peaks correspond to a bright spot like those shown in Fig. 37(b). Note how each plot lacks of any abrupt intensity variation on intensity from peak to another like those of Fig. 36(c), that is because there are no contributions from diffraction coming from the edges of the pyramidal prism.

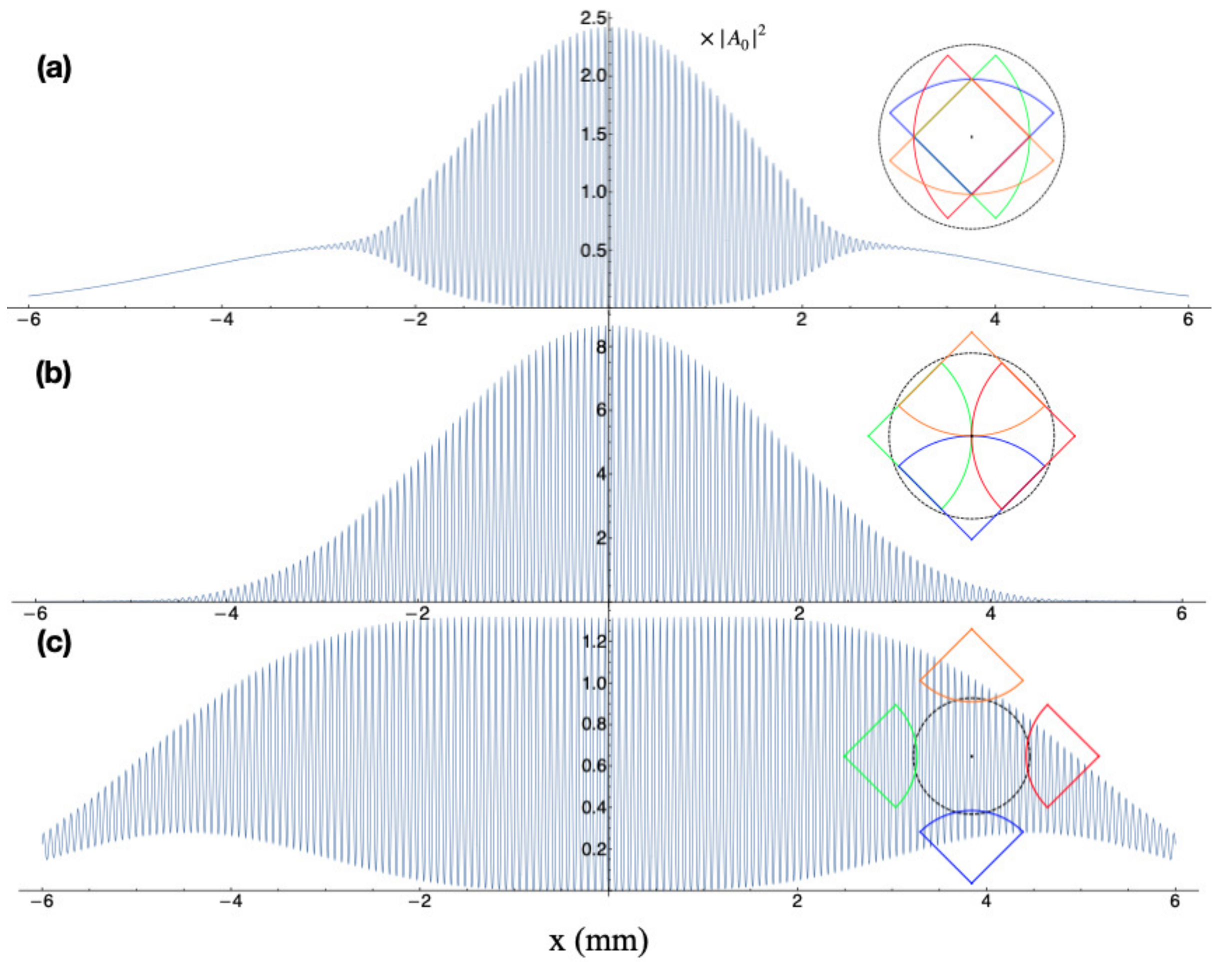

Figure 38. Results for an HG_{11} mode illuminating an acute prism with four faces, the intensity is evaluated at (a) $z = 286\,\mathrm{mm}$, (b) $z = 573\,\mathrm{mm}$, and (c) $z = 1.002\,\mathrm{mm}$, each case have as an inset to their right its corresponding overlap diagram. Parameters are $\lambda = 633\,\mathrm{nm}$, $w = 5.0\,\mathrm{mm}$, $\theta = 0.5^{\circ}$, and $R \to \infty$.

Chapter 8. Conclusions

This thesis work presented a numerical study of the light transmitted by symmetric pyramidal prisms. In the Fresnel approximation, the approaches presented use the symmetries present in the prisms to develop expressions for the diffracted amplitude that is ready to be evaluated numerically. The expressions are valid for an arbitrary number of prism faces and apply to acute or flat-topped prisms. The results significantly advance the restrictive and widely used plane wave models. Moreover, an effect not planned is the use of this approach as an optimization tool in which experimentally accessible parameters may vary until obtaining an optimal intensity pattern.

As part of the hypothesis, there was an active search for applying the developed results in optical trapping and lithography fields. In the context of structured light used in optical trapping, some cases produce arrays of bright spots with similar power, which could trap biological cells or microparticles simultaneously in multiple locations. These light distributions are created with high efficiency, which is significant given the losses that occur using other techniques. Other cases presented in this work produce uniform interference structures over broad areas, which can be helpful in lithography.

Generally, the intensity patterns obtained can be sized as desired, either by applying the scaling procedure described here or by using a lens to image the pattern at the desired magnification. Also, for a broader range of applications, it is possible to use the approach presented in this thesis to engineer intensity patterns with a wide variety of desired properties.

The presented results complied with the proposed objectives and went beyond the initial hypothesis. Specifically, the scaling factor and the spatial uniformity were a couple of results out of the initial loop of this work. This work lay the ground for the stable production of structured light.

This thesis work lays the ground for the stable production of structured light using robust optical elements. It opens the door for applications beyond the scope of the authors as the field of structured light is continually evolving towards four-dimensional spatiotemporal structured light and multidimensional quantum states, beyond orbital angular momentum towards control of all degrees of freedom, and beyond linear interactions, particularly for high-harmonic structured light Forbes *et al.* (2021).

8.1 Future Work

In closing, the taken approach used the usual Fresnel scalar amplitude formulation. Nevertheless, to produce nanostructures in lithography, the prism refraction angles can be so large that the scalar theory may not be appropriate in the interference region. One must instead use the *vector* amplitudes in the interference terms, having the form of the real part of $\vec{E}_i \cdot \vec{E}_j^*$, where $\vec{E}_i$ is the vector field produced by the ith prism face Burrow and Gaylord (2011). The theory developed here by simply assigning appropriate field directions to the terms of Eq. (17), and then computing the intensity with interference terms of the correct form may be readily adapted. It is also possible to work with other higher-order modes, *e.g.*, Hermite-Gaussian, Laguerre-Gaussian beams, and study its variation in intensity along the propagation axis.

Bibliography

Akhlaghi, E. A., Saber, A., and Abbasi, Z. 2018. Fresnel diffraction due to phase gradient singularity. *Optics Letters*, 43(12).

Brundrett, D., Gaylord, T., and Glytsis, E. 1998. Polarizing mirror/absorber for visible wavelengths based on a silicon subwavelength grating: Design and fabrication. *Applied Optics*, 37: 2534–2541.

Burrow, G. M. and Gaylord, T. K. 2011. Multi-beam interference advances and applications: Nano-electronics, photonic crystals, metamaterials, subwavelength structures, optical trapping, and biomedical structures. *Micromachines*, 2: 221–257.

de Boor, J., Geyer, N., Gosele, U., and Schmidt, V. 2009. Three-beam interference lithography: Upgrading a Lloyd's interferometer for single-exposure hexagonal patterning. *Optics Letters*, 34: 1783–1785.

de Boor, J., Dong Sik, K., , and Schmidt, V. 2010. Sub-50 nm patterning by immersion interference lithography using a littrow prism as a Lloyd's interferometer. *Optics Letters*, 35: 3450–3452.

Forbes, A., Oliveira, M., and Dennis, M. R. 2021. Structured light. *Nature Photonics*, 15: 253–262.

Goodman, J. 2017. *Introduction to Fourier Optics*. McGraw-Hill physical and quantum electronics series. W. H. Freeman.

Guan, Y. and Pedraza, A. 2004. Synthesis and characterization of self-organized nanostructure arrays generated by laser irradiation. *Materials Research Society Symposium Proceeding*, 818: 335–340.

Jenkins, F. and White, H. 1976. *Fundamentals of Optics*. McGraw-Hill physical and quantum electronics series. McGraw-Hill.

Jeon, T., Kim, D. H., and Park, S. G. 2018. Holographic fabrication of 3d nanostructures. *Adv. Mater. Interfaces*, 5: 1800330.

Ji-Hyun, J., Chaitanya, U., Martin, M., Taras, G., Steven, K., Yang, K. C., and L, T. E. 2007. 3d micro- and nanostructures via interference lithography. *Adv. Funct. Mater*, 24(17): 3027–3041.

Jiang, G., Shen, K., and Wang, M. R. 2013. Fabrication of 3d micro- and nano-structures by prism-assisted uv and holographic lithography. *Updates in Advanced Lithography*, pp. 227–252.

Juodkazis, S., Mizeikis, V., and Misawa, H. 2009. Three-dimensional microfabrication of materials by femtosecond lasers for photonics applications. *J. Appl. Phys.*, 106: 051101.

Kondo, T., Matsuo, S., Juodkazis, S., and Misawa, H. 2001. Femtosecond laser interference technique with diffractive beam splitter for fabrication of three-dimensional photonic crystals. *Applied Physics Letters*, 79: 725–727.

Lei, M., Baoli, Y., and Romano, A. R. 2006. Structuring by multi-beam interference using symmetric pyramids. *Optics Express*, 14(12): 5803–5811.

Mai, X., Moshrefzadeh, R., Gibson, U., Stegeman, G., and Seaton, C.1985. Simple versatile method for fabricating guided-wave grating. *Applied Optics*, 24: 3155–3161.

McGloin, D. and Dholakia, K. 2005. Bessel beams: diffraction in a new light. *Contemporary Physics*, 46: 15–28.

Ochoa, C. I., Garces, V., and O'Donnell, K. A. 2021. Generation of structured light using pyramidal prisms. *Applied Optics*, 60: 8882–8889.

Otte, E. and Denz, C. 2020. Optical trapping gets structure: structured light for advanced optical manipulation. *Appl. Phys. Rev.*, 7: 041308.

Pang, Y. K., Lee, J. C. W., Ho, C. T., and Tam, W. Y. 2006. Realization of woodpile structure using optical interference holography. *Opt. Express*, 14: 9113–9119.

Park, S. G. and Yang, S. M. 2013. Multicolor patterning using holographic woodpile photonic crystals at visible wavelengths. *Nanoscale*, 5: 4110.

Rubinsztein-Dunlop, H., Forbes, A., Berry, M. V., Dennis, M. R., D. L. Andrews, M. M., Denz, C., Alpmann, C., Banzer, P., Bauer, T., Karimi, E., Marrucci, L., Padgett, M., Ritsch-Marte, M., Litchinitser, N. M., Bigelow, N. P., Rosales-Guzmán, C., Belmonte, A., Torres, J. P., Neely, T. W., Baker, M., Gordon, R., Stilgoe, A. B., Romero, J., White, A. G., Fickler, R., Willner, A. E., Xie, G., McMorran, B., and Weiner, A. M. 2017. Roadmap on structured light. *J. Opt.*, 19: 0130001.

Saleh, B. E. A. and Teich, M. C. 1991. *Fundamentals of Photonics*. Wiley-Interscience.

Savas, T., Shah, S., Schattenburg, M., Carter, J., and Smith, H. 1995. Achromatic interferometric lithography for 100-nm-period gratings and grids. *Journal Vaccum Science and Technology B*, 13: 2732–2735.

Schonbrun, E., Piestun, R., Jordan, P., Cooper, J., Wulff, K. D., Courtial, J., and Padgett, M. 2005. 3d interferometric optical tweezers using a single spatial light modulator. *Optics Express*, 13(10): 3777.

Stay, J., Burrow, G., and Gaylord, T. 2011. Three-beam interference lithography methodology. *Rev. Sci. Instrum.*, 82: 023115.

Wang, G., Tan, C., Yi, Y., and Shan, H. 2003. Holography for one-step fabrication of three-dimensional metallodielectric photonic crystals with a single continuous wavelength laser beam. *J. Mod. Opt.*, 50: 2155–2161.

Wu, L., Zhong, Y., Chan, C. T., and Wong, K. S. 2005. Fabrication of large area two- and three-dimensional polymer photonic crystals using single refracting prism holographic lithography. *Appl. Phys. Lett.*, 86: 241102.

Yang, Y., Ren, Y. X., Chen, M., Arita, Y., and Rosales-Guzman, C. 2021. Optical trapping with structured light: a review. *Adv. Phot.*, 3: 034001.